8

Experimental Fragmentation

A number of studies over the intervening years since Mott's seminal theoretical efforts in dynamic fragmentation have been undertaken which allow testing of his theories. Some were pursued specifically for that purpose. Others were undertaken for other applications, but nonetheless provide useful test data for examining aspects of the theory.

Selected experiment studies are examined in the present section and compared with the fragmentation theory of Mott. This selection is, of course, not exhaustive. We will show that many of the theoretical concepts introduced stand up well to experimental scrutiny. Certain mysteries remain unresolved, however, and provide the challenge for yet more advanced theoretical efforts in fragmentation.

8.1 Olsen Expanding Ring

The expanding ring experiment to test the dynamic deformation and failure properties of engineering metals has continued to be pursued at Lawrence Livermore National Laboratory (LLNL) [Gourdin, 1989; Gourdin et al., 1989]. Extended development of the ring method provided an effective technique for assessing the dynamic tensile strength and strain-to-fracture properties, as well as the statistical fracture and fragmentation characteristics of the material. Here, we focus on extensive dynamic data obtained with the technique on uranium-6%-niobium (U6Nb) metal [Olsen, 2000; Grady and Olsen, 2003]. Data for this study were examined in an earlier section. Here a more thorough examination of the test method and the experimental results is undertaken.

8.1.1 The Experimental Method

Expanding ring tests were performed on machined U6Nb rings subjected to selected metallurgical heat treatment. Test samples were rings 34.4 mm inner

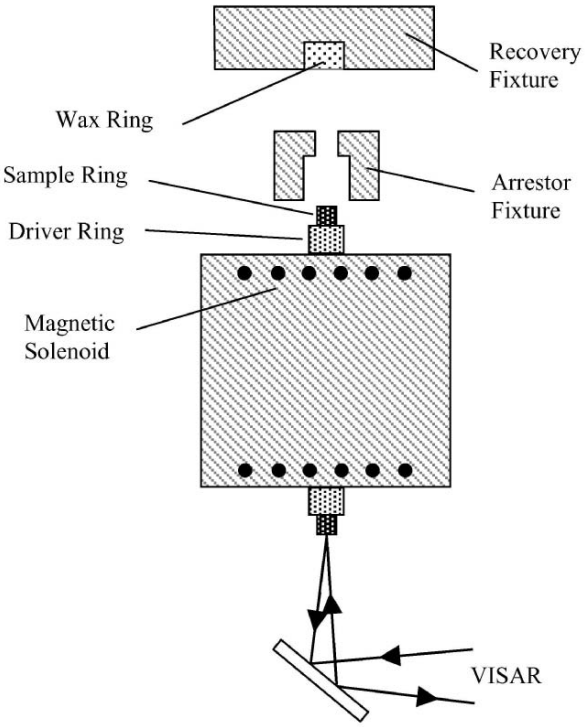

Fig. 8.1. Test configuration and diagnostics for expanding metal ring experiments are illustrated schematically

diameter and square cross section 0.76 mm on a side. The test configuration is illustrated schematically in Fig. 8.1.

The magnetic field excited by pulsing an electric current through a solenoid accelerates a metal driver ring and sample (U6Nb) ring radially outward. Expansion velocities ranging from about 100 to 300 m/s are achieved depending on the current amplitude. An arrestor fixture stops the driver permitting continued free flight of the sample ring. Velocity history of the ring is determined from time resolved velocity, or VISAR, measurements [Barker and Hollenbach, 1972] of the motion at one point on the ring. Free flight of the test ring is allowed through onset of fracture and fragmentation. Broken ring fragments are arrested and recovered within a stationary wax cavity in the experimental test fixture.

8.1.2 The Experimental Results

As noted, velocity histories of the U6Nb rings were measured with time-resolved velocity interferometry. Measured deceleration of the freely expanding ring prior to fragmentation, was used to calculate tensile flow stress of

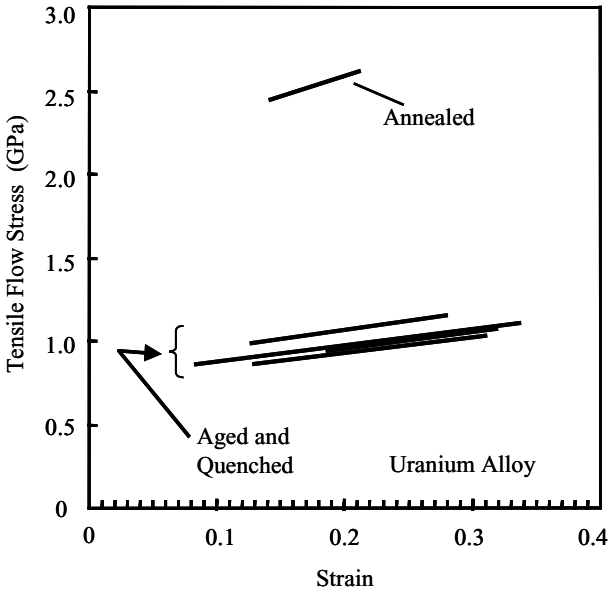

Fig. 8.2. Selected tensile stress versus strain to failure at an expansion rate of approximately $1.3 \times 10^4/\mathrm{s}$

the ring up to the time of fracture. Tensile stress, as a function of strain, for several aged and one annealed test sample is shown in Fig. 8.2. Strain rate during the free expansion deformation was approximately $1.3 \times 10^4/\mathrm{s}$. Tensile stress for the several aged samples was approximately 1.0 GPa to a fracture strain (increase in radius) of about 30%. On the other hand, the one annealed ring specimen exhibited a tensile flow stress of about 2.5 GPa and failed at a somewhat earlier 20% strain.

In each test the number of fragments produced (equivalently, the number of fractures) was determined. Fragment number versus the expansion velocity at fragmentation are shown for the series of U6Nb expanding ring experiments in Fig. 8.3. The anomalous point high on the graph is the one test on a markedly differently heat treated U6Nb sample identified as annealed in Fig. 8.2 and is discussed further, later in this section. A least squares fit, excluding the one anomalous point, provided the power law representation of the data shown in Fig. 8.3. Dynamic toughness data for the same data in Fig. 8.3, as calculated through the energy-based relation relating fragment number to toughness,

$$N = \left(\frac{\rho c \dot{\varepsilon}}{\sqrt{12} K_f} \right)^{2/3} , \tag{8.1}$$

are shown in Fig. 8.4.

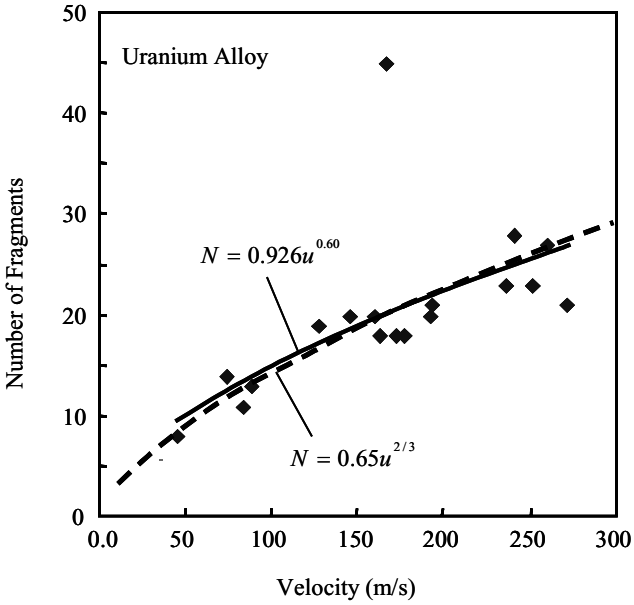

Fig. 8.3. Fragment number versus expansion velocity at fracture for U6Nb expanding ring fragmentation tests

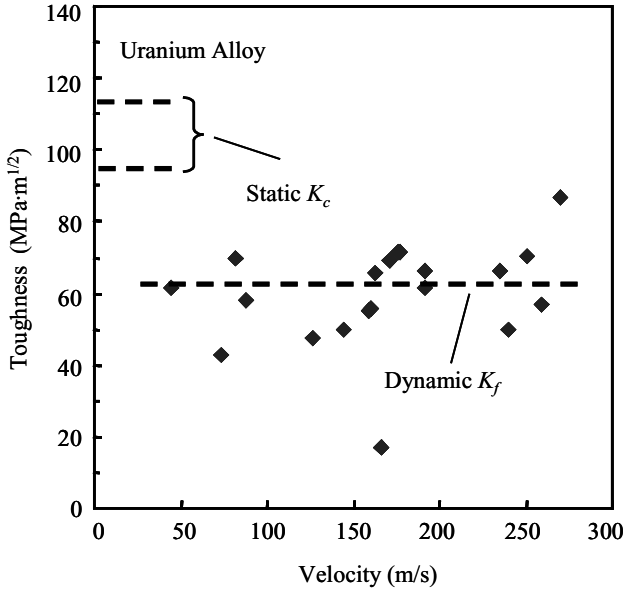

Fig. 8.4. Dynamic fragmentation toughness calculated through theoretical relation relating fragment number, expansion rate and material toughness

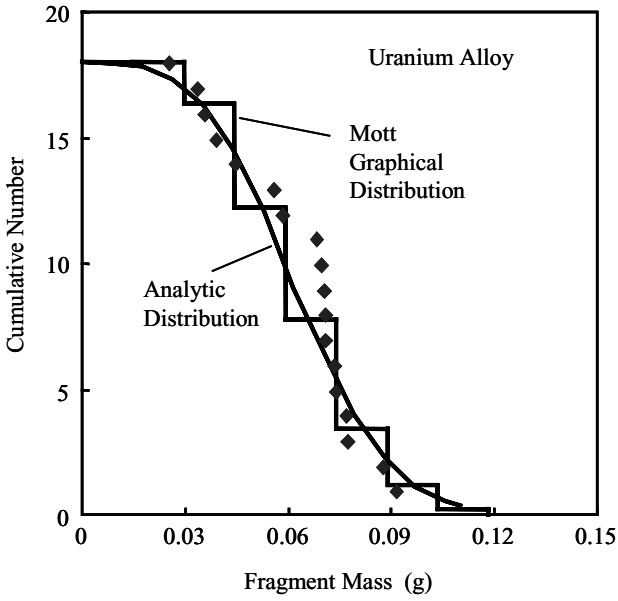

Fig. 8.5. Comparison of cumulative fragment distribution for one representative U6Nb expanding ring fragmentation test with the theoretical Mott fragment size distribution

In one representative test each fragment was separately weighed and the cumulative fragment size distribution shown in Fig. 8.5 was obtained. The data presented in Figs. 8.2 through 8.5 are also provided in Table 8.1.

8.1.3 Some Experimental Observations

The present study of dynamic fragmentation is afforded invaluable insight through a more in-depth examination of the expanding ring experimental fragmentation results. A metallographic image of a representative fracture is shown in Fig. 8.6. The outer deformed surface of the stretched ring exhibits an undulating, uneven surface characteristic of heterogeneous slip-line plasticity. The reduced area of the fracture surface points to a pre-fracture deformation localization through plastic necking. The failure process is completed through pervasive ductile extension fracture through the narrowest portion of the necking region. Arrested necking regions were also observed in a number of the recovered fragments.

Ductile deformation, through dimple plasticity, is clearly evident in the expanded image of the fracture surface shown in the upper fractograph in Fig. 8.7. The dimple morphology appears tri-modal. Dimple sizes range from 2–3 μm for the smallest up to 15–30 μm for the largest. Inclusions observed within larger dimples are probably fracture initiation sites. Dimple size may reflect local fracture speed in the failure process.

Table 8.1. Expanding ring fracture and fragmentation data

Test Number	Velocity at Failure (m/s)	Expansion at Failure (%)	Stress at Failure (GPa)	Number of Fragments	Cumulative Distribution Mass (g)	Num.
22	87.9	–	13	13	0.092	1
42	82.3	0.88	11	11	0.088	2
44	45.1	0.77	8	8	0.078	3
30	73.1	0.9	14	14	0.077	4
14	144.9	0.89	20	20	0.074	5
24	177.9	1.1	18	18	0.074	6
20	192.1	1.18	21	21	0.071	7
16	126.5	–	19	19	0.071	8
26	176.2	1.05	18	18	0.070	9
52	162.2	1.15	18	18	0.069	10
54	160.4	0.89	20	20	0.068	11
10	191.7	0.95	20	20	0.058	12
56	250.8	0.97	23	23	0.056	13
60	239.6	1.15	1.16	28	0.044	14
28	165.7	21	2.65	45	0.039	15
62	171.5	31.7	1.08	18	0.035	16
66	159.4	31.1	1.03	20	0.033	17
68	235.5	31.9	1.01	23	0.025	18
70	259.4	20.7	1.2	27		

The failure morphology shown in Fig. 8.6 and the expanded view of the fracture surface in the upper picture in Fig. 8.7 is illustrative of the fracture data examined in the present theoretical study. Data from these tests fall within the scatter of the curve shown in the fragment number plot in Fig. 8.3 even though these data represent materials subjected to several different aging treatments. All, however, were quenched from elevated temperature leaving the metal in the more ductile alpha phase. The modestly different aging treatments shows no apparent influence on either the fracture behavior or the fragmentation statistics.

The present fracture behavior of quenched U6Nb shows marked similarity to observations of spall fracture in U6Nb [Hixson, et al. 2000, and Zurek, et al. 2000]. Similarities extend to both the character of dimple plasticity on fracture surfaces and identification of carbide inclusion fracture initiation sites in higher resolution metallography. The similarity is not surprising in that strain rates at fracture in necking regions of the expanding ring tests exceed 10^4/s, approaching that of the spall experiments. Additionally, tensile stress triaxiality is amplified within necking regions again approaching conditions comparable to the spall experiment.

The anomalous data point observed in Figs. 8.2 through 8.4 corresponds, in contrast, to a sample in which the heat treatment left most of the metal in

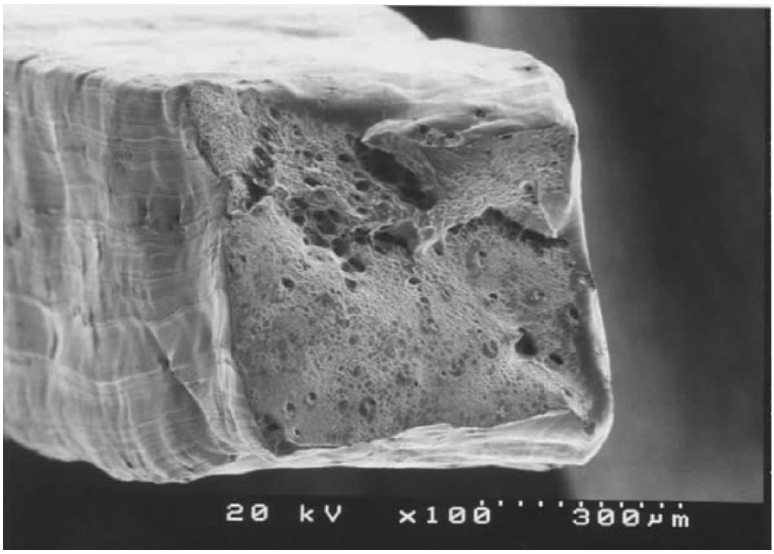

Fig. 8.6. Expanding ring dynamic fracture characteristics

the more brittle gamma phase. A corresponding fractograph of the fracture surface from the ring experiment on this sample is shown in the lower image of Fig. 8.7. The predominantly cleavage fracture character differs starkly from that of the more ductile fracture in the alpha phase material shown above (actually a variant α'' of the alpha phase, e.g., Addessio, et al. (2003)).

The expanding ring experiment is also unique, in providing a uniformly straining dynamic unconfined tension experiment, in which both tensile stress and plastic strain can be readily measured. Both stress and strain are determined in the present tests through velocity interferometry measurements of the radial velocity history. The effective measurement duration occurs from the time of decouple from the driving, current-carrying ring to the time of localization onset and failure. Strain and strain rate within this measurement period are provided by the velocity and displacement history. Stress is determined from the deceleration of free expansion through solution of the governing momentum equations.

Measured stress versus strain histories provided in Fig. 8.2 for selected experiments include several alpha phase materials subjected to different aging treatments and the one test on predominantly gamma phase metal. As previously stated, rings of the alpha phase materials achieve a dynamic flow stress of approximately 1.0 GPa before failing at expansions approaching 30% and higher. It should also be emphasized that failure in these materials proceeds first through deformation localization and ductile necking, and subsequently by extension fracture. Numerous arrested necking regions were observed in recovered fragments.

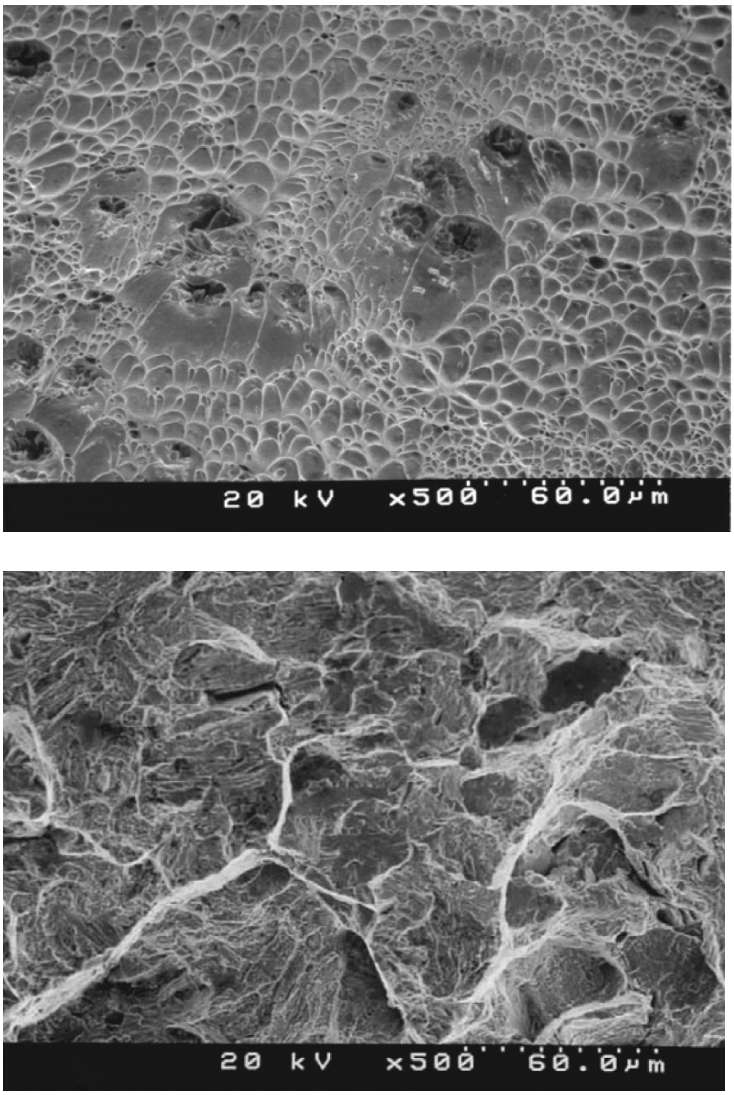

Fig. 8.7. Fractography of fracture surfaces for predominantly alpha phase (upper photo) and gamma phase (lower photo) U6Nb expanding ring samples

The test on the largely gamma phase U6Nb sample exhibited, in contrast, a dynamic flow stress well in excess of 2 GPa and a markedly reduced strain to failure (Fig. 8.2). Further evidence for the starkly more brittle character of dynamic fracture of U6Nb in this preparation is provided by the significantly reduced indications of ductile necking preceding extension fracture, clear indications of cleavage fracture as evident in Fig. 8.7, the larger number of fragments shown in Fig. 8.3 and the correspondingly

reduced fracture energy provided in Fig. 8.4. Although a static fracture toughness value for the present predominantly gamma phase metal was not available, an appreciable reduction from the alpha phase material would be expected.

A final comment on the comparison of the dynamic toughness inferred through the energy-based theory with the static fracture toughness in Fig. 8.5 is warranted. The reasonably close agreement between the dynamic and static values is remarkable and speaks strongly for an energy-controlled mechanism governing the characteristic fracture spacing and fragment number. On the other hand, one may question why they differ by almost a factor of two. First, there is a number of simplifying theoretical assumptions in the quantitative development of the energy theory which could readily account for the difference. But putting these explanations aside, there is an interesting material issue which could easily contribute to the difference. Dissipation resulting from the propagation of a through-going fracture in an engineering size sample of metal accounts for the observed fracture toughness of the material. Dissipation on the fracture surface is heterogeneous on some length scale, however dissipation at any point on the surface may exceed or be less than the average. The present metal rings with substantially less than a square millimeter cross section, combined with the statistical selectivity of weaker fracture sites, could lead to effectively lower dynamic fracture energy, as is observed. This possible material dependent difference would suggest something other than geometric scaling if the size of the test rings were varied. This complication has not been explored.

8.2 Grady and Benson Expanding Ring

The expanding ring fragmentation study on U6Nb metal described in the previous section nicely supports features of both Mott's statistical theory and the energy-based theory of dynamic fragmentation, and offers ideas for merging the two theories, as was pursued in Chap. 5. Here we will discuss earlier expanding ring tests of Grady and Benson (1983) in which the experimental results do not as tidily support the theoretical predictions. These experiments, in fact, motivated the experimental efforts of LLNL from which the reported study on U6Nb metal emerged. This previous work was in turn stimulated by even earlier experiments using explosives to drive expanding rings [Perrone, 1968; Hoggatt and Recht, 1969; Warnes et al., 1981] and magnetic loading methods [Walling and Forrestal, 1973].

8.2.1 The Experimental Method

The experimental method used in the study is described in detail in Grady and Benson (1983) with further analysis of the data provided in Grady

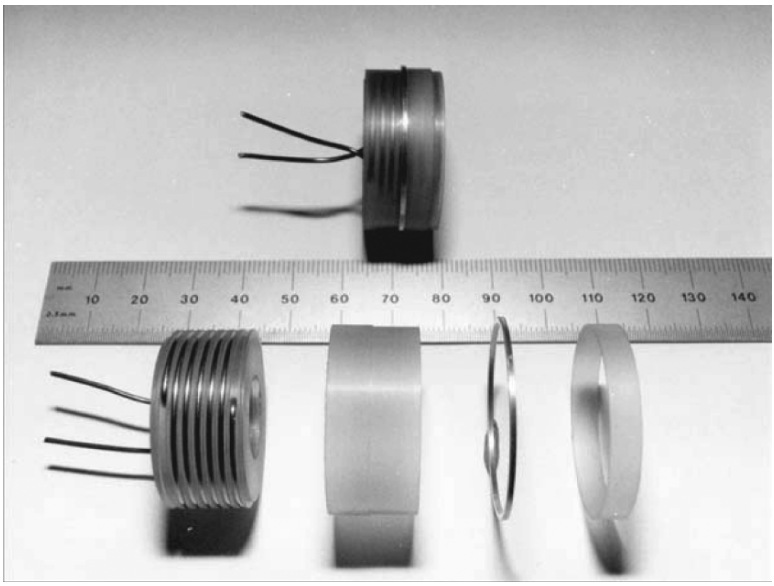

Fig. 8.8. Electromagnetic launch experiment illustrating assembled test (*top*) and assembly component parts (*bottom*) including, launching solenoid test ring and insulating plastic support pieces [Grady and Benson, 1983]

et al. (1984) and Kipp and Grady (1985, 1986). Briefly, a fast-discharge pulsed-power system was used to electromagnetically accelerate metal rings in a radially expanding geometry. The test assembly is illustrated in Fig. 8.8 in which the solonoidal coil carrying the driving current is sheathed with supporting, and insulating, plastic cylindrical sections and the test metal ring. The technique provided uniform radial acceleration of the ring to velocities of several hundred meters per second, although a slight figure-of-eight motion was imparted presumably due to the helicity of the driving coil. Another down side to the technique was an induced electric current in the test ring and the uncertain influence of inductive heating on the plastic flow and fracture properties of the metal. Estimates of heating are provided in the paper of Grady and Benson (1983).

Acceleration history and the velocity at fracture were measured with streak-camera methods. A variety of experiments were performed on aluminum and copper rings to assess the statistical fragmentation properties, including, the strain-to-fracture, the number and size statistics of fragments created, and details of the fracture process. Both the soft OFHC and the 1100-O aluminum selected for testing in the study fractured in dynamic tension through ductile necking followed by extension fracture at a late stage in the necking process. Representative fracture and arrested necking behavior in the dynamic tests are illustrated for the aluminum in Fig. 8.9. Static tension tests were also performed on comparable sized dog-bone shaped specimens.

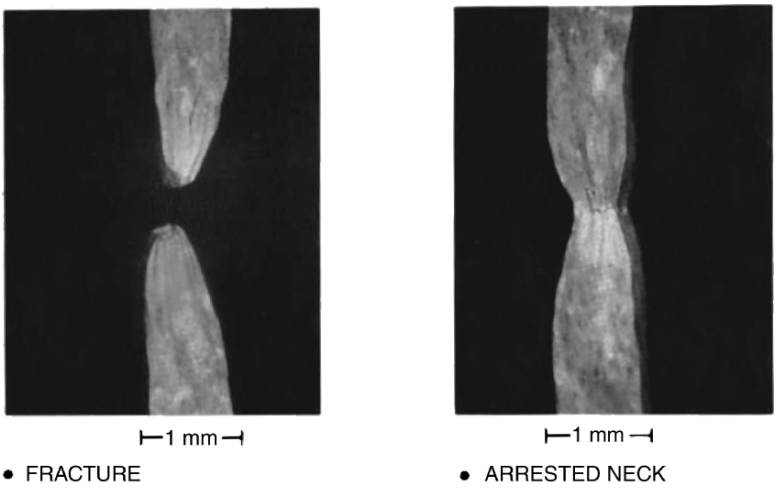

Fig. 8.9. Expanding ring fracture characteristics on 1100-O aluminum illustrating a completed fracture (*left*) and an arrested neck (*right*) [Grady and Benson, 1983]

8.2.2 Fragment Number Experiments

A series of fragmenting ring experiments was performed on 1100-O aluminum and soft OFHC copper, where the initial capacitor voltage was selected to vary the strain rate at the time of fracture. Velocities ranging from about 20 to 200 m/s were achieved which corresponded to strain rates from about 10^3/s to 10^4/s. At the lowest voltages it was not uncommon to recover markedly expanded, but unfractured rings. In these experiments, the number of fragments from each test were counted and correlated with the expansion velocity at fracture. These data are plotted in Fig. 8.10.

Clearly, fragment number data for ring fragmentation of these two ductile metals is better described by a linear dependence on expansion velocity. This behavior contrasts with the two-thirds power dependence observed for the U6Nb ring data. In searching for a possible experimental reason for the different behavior, electric current flow in the fragmenting aluminum and copper rings is a possible suspect. A pusher ring was used in the technique to fragment the U6Nb rings keeping residual electric currents to a minimum. Increasing currents at the higher driving velocities might be expected to influence breakup through excessive heating in the thinning fracture zones.

Ignoring this complication, the functional trend of the fragment number versus velocity for the soft aluminum and copper data is better captured with the earlier Mott statistical prediction of fragment number than with the energy-based prediction. Working with relations developed earlier, fragment number per unit length is provided by,

$$N = \sqrt{\frac{\rho\dot{\varepsilon}^2}{2\pi Y}\frac{n}{\sigma}}\,. \tag{8.2}$$

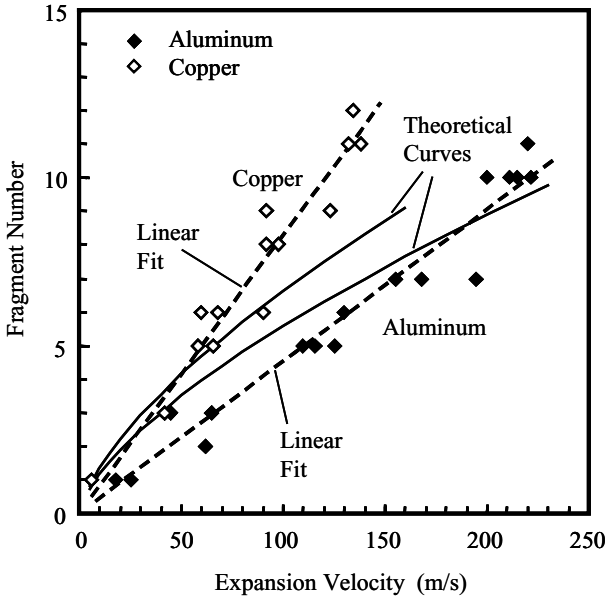

Fig. 8.10. Fragment number data for aluminum and copper ring tests. Curves are the least squares linear fits and predictions from energy-based fragmentation theory

Equation (8.2) is appropriate for sensibly large n, and N is determined by the statistical standard deviation in strain-to-fracture, ($\cong 1.28\sigma/n$) as well as the flow stress Y, metal density ρ and the expansion strain rate $\dot{\varepsilon}$. The ring is then predicted to break into a total number of fragments,

$$N_T = 2\pi RN = \left(\frac{2\pi\rho}{Y}\frac{n}{\sigma}\right)^{1/2} u \; . \tag{8.3}$$

A measure of the standard deviation in the strain-to-fracture is not known so a forward prediction of fragment number cannot be made. Linear fits to the data, shown in Fig. 8.10, can be made, however, and the necessary back calculation performed for the strain-to-fracture standard deviation calculated from (8.3). Values of 0.051 and 0.096 are obtained for copper and aluminum, respectively. The standard deviation in strain-to-fracture for copper is found to be about 12% of the measured static strain-to-fracture ($\simeq$0.4) and is not unreasonable. The calculated standard deviation in strain-to-fracture for aluminum is approximately equal to the static strain-to-fracture ($\simeq$0.1) and seems unreasonably large. Dynamic strains for this ductile aluminum are substantially larger, however, and considerations in the following subsection will show that this statistical failure measure is also sensible.

The corresponding total fragment number expression based on the fracture energy theory is,

$$N_T = 2\pi \left(\frac{\rho R}{24\Gamma} \right)^{1/3} u^{2/3} , \tag{8.4}$$

where Γ is the fracture energy. Equation (8.4) is clearly at odds with the functional dependence on the expansion velocity in Fig. 8.10. Nonetheless, predictions based on (8.4) are enlightening. The fracture energy Γ for the two metals was estimated from the measured static tensile flow stress at fracture and the deformation strain in the fracture zone inferred from the geometry of the neck and fracture deformation. Values of $\Gamma = 0.03$ MJ/m^2 for aluminum and $\Gamma = 0.07$ MJ/m^2 for copper were calculated and are probably reasonable within $\pm 50\%$. The values for Γ correspond to effective fracture toughness of 60 MPa·m$^{1/2}$ and 140 MPa·m$^{1/2}$ for aluminum and copper, respectively. Fragment number curves based on (8.4) are shown with the data in Fig. 8.10 and, although functionally wrong, the reasonable agreement in magnitude is encouraging. An interesting feature to ponder is the scale dependence of the energy-based relation (dependence on the ring radius R) in comparison to the scale independence of the Mott relation in (8.3). This scale dependence has not been explored in any of the previous ring studies.

A fascinating observation is provided by the plot shown in Fig. 8.11, where the fragment number data for both aluminum and copper are plotted as a function of the radial kinetic enrgy, $\rho u^2/2$. It is remarkable that the data are effectively collapsed in this plot. The curve is a best fit of the fragment number to the kinetic energy of the form $N_T = (T/\tau)^{1/2}$ with a value of $\tau = 64$ MJ/m^3. Both the statistical Mott and the energy-based relations for fragment number in (8.3) and (8.4) contain ρu^2 in the numerator. Overlay of the two data sets in Fig. 8.11 then requires that the corresponding governing fracture properties in either theory for the two materials scale to effect the invariance. This overlay of the data could certainly be fortuitous but it is certainly intriguing and warrants further study.

8.2.3 Fracture Strain Experiments

A further intriguing feature of the dynamic expanding ring experiments is plastic strain accumulated in the metal up to the point of fracture and fragmentation. In the work of Olsen (2000) in the previous section on U6Nb this strain was simply determined by the amount of expansion incurred at the point of fracture as determined through the VISAR velocity history measurements. In the present study strain to fracture was pursued in somewhat more depth.

Both of the ductile metals investigated in the present study exhibit substantial hardening in tension, and static strains-to-fracture of approximately 0.08 and 0.40 were measure for the ductile aluminum and copper, respectively. These static values provide a reference for examining the strains accumulated in the dynamic fracture process.

Before investigating the experimental results of the expanding ring tests of Grady and Benson (1983), it is instructive to examine the fracture strain

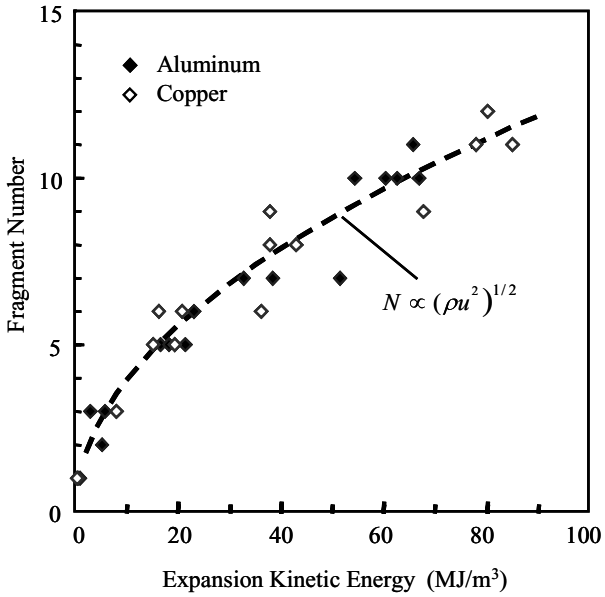

Fig. 8.11. Fragment number data plotted against expansion kinetic energy $\rho u^2/2$

behavior inferred from the several theories pursued here. Fracture in the Mott theory is characterized by a statistical strain-to-fracture and the cumulative strain-at-fracture completion is provided by the integral,

$$\varepsilon_f = \int_0^\infty (1 - D)\dot{\varepsilon} dt \ . \tag{8.5}$$

The factor of $1 - D$ accounts for the fraction of the length over which straining has arrested due to the propagation of Mott release waves from sites of fracture. This factor is provided by,

$$1 - D = e^{-\int \lambda(\varepsilon) d\varepsilon} \ . \tag{8.6}$$

A power law representation of $\lambda(\varepsilon)$, which has been pursued extensively in the present text, provides a Weibull description of the strain-to-fracture statistics. Alternatively, an exponential representation, and Gumbel statistics, as was pursued by Mott, could be used. Weibull statistics leads to a cumulative failure strain in (8.5) of,

$$\varepsilon_f = \alpha_n \left(\frac{\sigma^n}{\sqrt{2Y/\rho\dot{\varepsilon}^2}} \right)^{\frac{2}{2n+1}} \ . \tag{8.7}$$

For small values of the distribution shape parameter n the failure strain in (8.7) exhibits a more complex dependence on properties. (For $n = 1$ a dependence on strain rate of $\varepsilon_f \sim \dot{\varepsilon}^{2/3}$ is predicted.) However, for sensibly large n,

as is expected to be the case, (8.7) approaches $\varepsilon_f \cong \sigma$, and failure strain is effectively independent of the expansion rate, as well as other governing material properties. The Mott approach using Gumbel statistics leads immediately to a rate independent cumulative failure strain.

In the energy-based approach to fragmentation, the theory examines a representative fracture from fracture inception until completion. It was shown in Sect. 3 that, if the fracture resistance is characterized by a dissipation energy Γ, a time,

$$t_f = \left(\frac{72\rho\Gamma^2}{Y^3\dot{\varepsilon}} \right)^{1/3} , \tag{8.8}$$

is required for fracture completion and within this time a Mott release wave propagates a distance,

$$x_f = \left(\frac{3\Gamma}{\rho\dot{\varepsilon}^2} \right)^{1/3} , \tag{8.9}$$

from the fracture. Within this region a nominal strain,

$$\varepsilon_f = \varepsilon_{fo} + \int_0^{t_f} \dot{\varepsilon} dt , \tag{8.10}$$

is achieved, where ε_{fo} is the strain at fracture onset. Equation (8.10) yields,

$$\varepsilon_f = \varepsilon_{fo} + \left(\frac{72\rho\Gamma^2\dot{\varepsilon}^2}{Y^3} \right)^{1/3} , \tag{8.11}$$

and, if the onset of fracture strain ε_{fo} is independent of strain rate, a two-thirds power dependence on strain rate is expected, with a quantitative prediction provided by (8.11) if the material parameters governing Mott fragmentation are known.

There are various methods for assessing the fracture strain in the present expanding ring experiments and two of these methods are explored here. First, it was convenient to soft capture all of the fragments, measure the total length $L = \sum L_i$ of the fragments, and identify a fracture strain $\varepsilon_f = 1 - L/L_o$, where L_o is the initial circumferential length of the test ring. This strain measure is plotted as a function of expansion velocity in Fig. 8.12 for the same copper and aluminum fragmenting ring fragment number data shown in Figs. 8.10 and 8.11.

Curves through the data are based on (8.11) and values of Y and Γ determined from the static tension tests. Fracture onset strain ε_{fo} was selected to best fit the fracture data. This estimate of ε_{fo} is somewhat larger than the static tensile strain-to-fracture for the two metals. For contrast, the strain rate independent fracture strain intrinsic to the Mott theory is also illustrated.

The various comparisons in Fig. 8.12 certainly raise questions concerning the accumulation of strain up to and during the expanding ring breakup

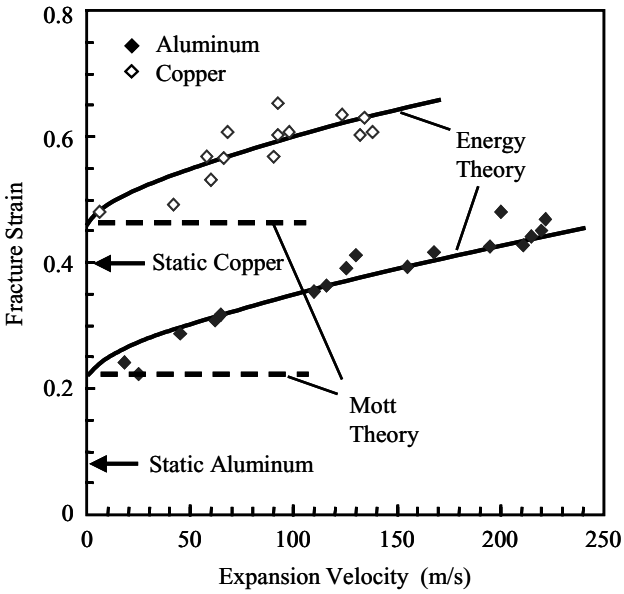

Fig. 8.12. Strain at fragmentation for aluminum and copper rings. Comparisons with energy-based and Mott theories are shown along with measured static strain-to-fracture

process. Intrinsic rate dependence during deformation leading up to the fracture process is certainly possible and could account for the observations within the context of the Mott statistical theory. Nevertheless, the reasonably close quantitative agreement of the measured excess strain with predictions based on the energy theory suggests that at least some of the features of the additional cumulative straining implied by the theory during the time-dependent fracture process are probably correct.

An alternative method for determining the strain-to-fracture in the ring experiments is to interrogate the accumulated strain in individual fragments. This can be done by both weighing each individual fragment and measuring its length. The extension, or fracture strain, corresponding to an individual fragment is provided by,

$$\frac{L}{L_o} = 1 + \varepsilon_f = \frac{L}{M}\frac{M_T}{2\pi R_o} \,, \tag{8.12}$$

where, L and M are the measured residual length and mass of the fragment, respectively, M_T the total mass of the ring, and $2\pi R_o$ the initial circumference of the ring. This approach was pursued in the earlier study [Grady and Benson, 1983], but was not reported in the publication of that study. Four fragments each were randomly selected from four separate tests conducted on the ductile aluminum at approximately the same expansion velocities (in the range of

310–350 m/s), and in which 12 to 13 fragments for each ring was achieved. (These were not the same experiments reported in Figs. 8.10–8.12.) Fragment extension determined through (8.12) is plotted against cumulative fragment number for the sixteen fragments in Fig. 8.13.

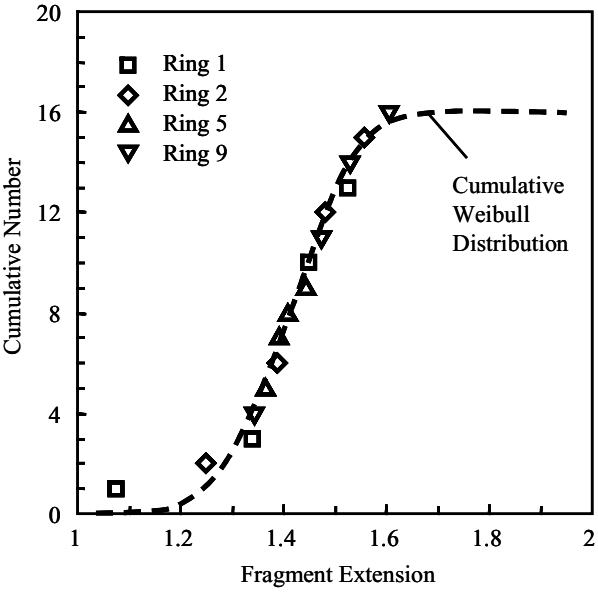

Fig. 8.13. Strain at fragmentation determined from the measured length and weight of individual aluminum fragments. A Weibull function is fit to the cumulative fragment number data

In this presentation of the data the recovered fragments showed a marked statistical spread in the strain-to-fracture. The distribution in Fig. 8.13 was fit to a cumulative Weibull distribution,

$$N(\varepsilon_f)/N_o = 1 - e^{-(\varepsilon_f/\sigma)^n} \ . \tag{8.13}$$

A best fit to the data provides a scale parameter $\sigma = 0.45$ and shape parameter of $n = 4.5$. A standard deviation in strain-to-fracture of approximately $1.28\sigma/n \cong 0.13$ is in reasonable agreement with the value of 0.096, previously back calculated from the fragment number data and the Mott relation in (8.3).

Thus, aspects of the Mott statistical theory are apparently playing a role in the breakup process. Namely, a statistical spread in the time, and strain, at which fractures achieve completion. This feature of the fracture process is further emphasized in the expanding tube experiments of Winter (1979) and the more recent tests of Vogler et al. (2003).

8.2.4 Fragment Size Statistics

Fragmentation of the expanding ring appears to be a random process. Both the breaks in the ring, as well as the well-defined necking regions constituting arrested fractures, appear to be statistically dispersed around the circumference of the ring. Fragments collected from any given test can vary in length by a factor of ten or more. This statistical fragmentation behavior was also noted in the expanding ring tests on U6Nb metal discussed in the previous subsection. Sensible agreement with the Mott treatment of the fragmentation statistics was found, although this was actually only quantified in the experimental study for one test.

The statistical distribution in fragment size (or length) was also explored in the present study. As in the case for fracture strain, there are different ways that the data can be displayed. For the one experiment on U6Nb a cumulative distribution in fragment size was presented. The number of fragments from that one test was too sparse to provide a meaningful density distribution.

In the present series of tests five experiment on 1100-O aluminum conducted at nominally the same expansion velocity, and in which 11 to 13 fragments each were produced, were combined and their collective density distribution was determined. A histogram of the fragment number versus mass is provided in Fig. 8.14. The mass intervals are 2.5 mg and, since aluminum density is approximately 2.7 mg/mm^3, each interval adds about one mm to the fragment length. The mode of the experimental distribution peaks somewhere in the range of 10–20 mg, and tails off for both larger and smaller fragments.

A best fit to the experimental data with both an exponential (Lineau) and an analytic Mott distribution is also shown in Fig. 8.14. The exponential distribution, as presented, is clearly at odds with the data. Note, however, that fragments at the small end of the distribution are within a factor of two to three times the initial cross section dimension of the metal ring (1 mm $\sim$ 2.7 mg). One might expect different physics to govern fracture at this length scale. Thus an exponential distribution with a tail off at the small fragment end due to this different physics might not be an unreasonable representation of the data.

The Mott distribution appears to be a better description of the data. Selecting rings with 11, 12 and 13 fragments probably unfairly broadens the distribution by about 10%. The several large fragments in the large end tail of the distribution are totally at odds with the Mott distribution, however.

Very distinct arrested necking regions such as shown in Fig. 8.9, were a conspicuous feature in the present expanding ring experiments. For the sake of interest a fragment size distribution for this same set of five tests was generated by also considering the well-defined necks as completed fractures. This distribution is provided in Fig. 8.15, and again compared with the Mott and the exponential Lineau theoretical representations of the data.

The Mott distribution does appear to capture the general trend of the experimental distribution. Again, however, it is not clear whether the decrease

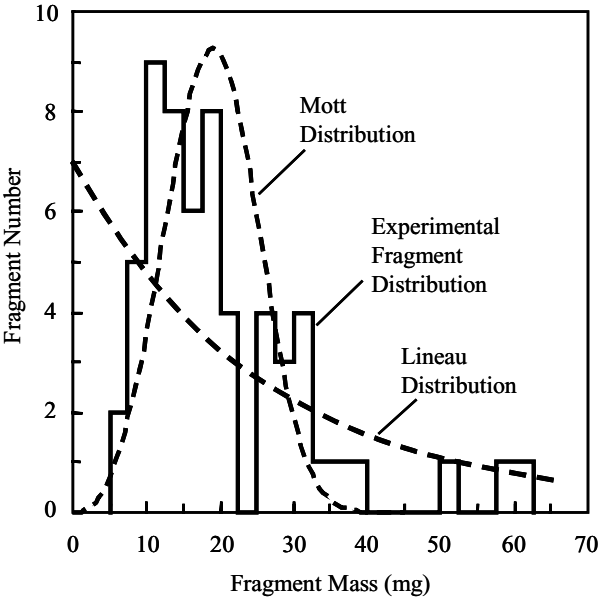

Fig. 8.14. A collective histogram of the fragments from five ring test on 1100-O aluminum in which 11 to 13 fragments were produced. The fragment mass in mg is approximately equal to the length in mm

in fragments at the small end of the distribution is due to the Mott interaction physics, or just due to the fact that fragment lengths are approaching the ring cross-section dimension. Also, as in the case of the fragment distribution in Fig. 8.14, there are several long segments of a size at odds with the Mott distribution.

It is also of interest to examine the fragment statistics over the wider range of expansion velocities achieved in the study. Representations of the fragment distributions such as shown in Fig. 8.14 become difficult, however, because of the limited number of fragments produced in some of the tests. One possible approach for examining the random nature of the fragmentation event is to pick a statistical measure in the spread of the fragments size, such as the standard deviation for each test, and compare this with the theoretically predicted standard deviation. This approach has been carried out for a limited number of the tests on 1100-O aluminum. For each ring fragmentation test the standard deviation is calculated and normalized by the average fragment size. This normalized standard deviation is plotted as a function of the number of fragments in each test in Fig. 8.16.

For comparison, the corresponding statistical measure is calculated for several of the theoretical distributions. The normalized standard deviation for the Lineau (exponential) distribution is unity. For some of the tests examined, the number of fragments produced was small (four in one – six in

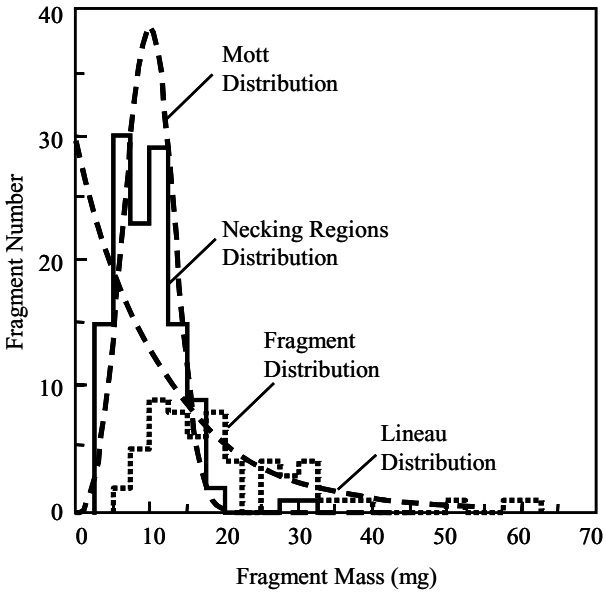

Fig. 8.15. A collective histogram for the same five ring test as the previous figure, where well defined arrested necks are also included in the partitioning of circumferential fragments

another). Consequently, it is sensible to calculate the same statistical parameter for the binomial distribution, which is equivalent to the Lineau distribution assumptions on a finite line length. The normalized standard deviation for the binomial distribution is also shown in Fig. 8.16. The normalized standard deviation of the Mott distribution ($\sim$0.321) is also shown in the Fig. 8.16.

Clearly, the experimental data are statistically tighter than predicted by a Lineau (or binomial) distribution. There is also a tendency for the standard deviation of the data to decrease with decreasing fragment number as suggested by the binomial distribution. The measured standard deviations are not, however, in agreement with the Mott distribution.

Usually it was an errant large fragment in the collection which markedly increased the experimental standard deviation, but not in every case. Nonetheless, the data disagree with the Mott prediction of the spread in fragment size by nearly a factor of two. So again, the present ring data suggest that the fragmentation process is more complex than the simpler theories predict.

8.3 Weisenberg and Sagartz Expanding Cylinder

An interesting experiment intermediate between the expanding ring tests discussed previously, and exploding cylinder tests considered in Sect. 7, was

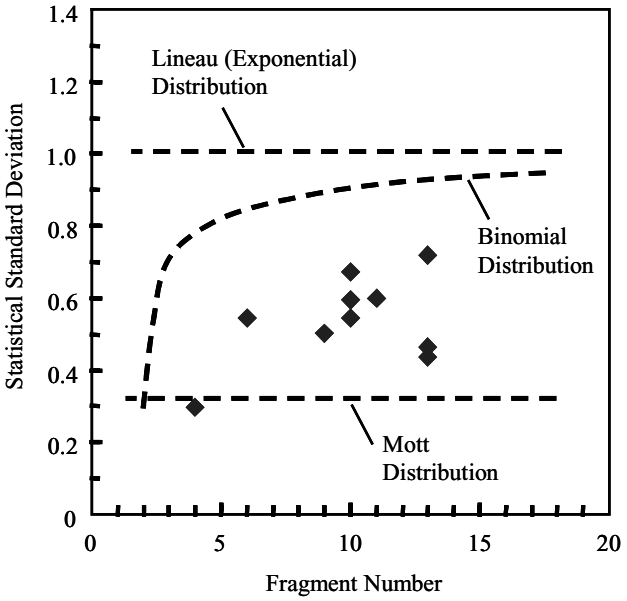

Fig. 8.16. Standard deviation normalized by the average fragment size plotted against the number of fragments produced in the test for the expanding ring fragmentation experiments on 1100-O aluminum

performed by Weisenberg and Sagartz (1977). In that study they used similar inductive methods powered by a large capacitor discharge system to rapidly expand and fracture thin cylinders of 6061-T6 aluminum. Current is carried by an internal copper conductor. The copper driver applies a radial driving pressure approaching 2 GPa for several microseconds accelerating the aluminum cylinder to its terminal radial velocity. Cylinders were 127 mm in diameter and 102 mm in length with a wall thickness of 1.27 mm. Dynamic fracture was observed photographically to occur at about 30% expansion strain and at a strain rate of approximately 10^4/s. This value is slightly below the approximately 40% strain in the 1100-O aluminum ring experiments in the previous section at a comparable strain rate.

During the deformation proceeding fracture, slip lines formed at angles of approximately 30° to the axis of the cylinder. Fracture then occurred along these slip lines and propagated until breakup was complete. Fragments from one test [Weisenberg and Sagartz, 1977] collected and displayed are shown in Fig. 8.17. The collection nicely illustrates the nature of the dynamic fracture process, including the tendency toward oblique fracture along plastic slip lines and arrested fractures due to unloading Mott waves. Details of the deformation processes leading to fracture are more readily observed in the high speed photograph of one cylinder test shown in Fig. 8.18.

Fig. 8.17. Fragments from one magnetic expanding cylinder test on 6061-T6 aluminum [Weisenberg and Sagartz, 1977]

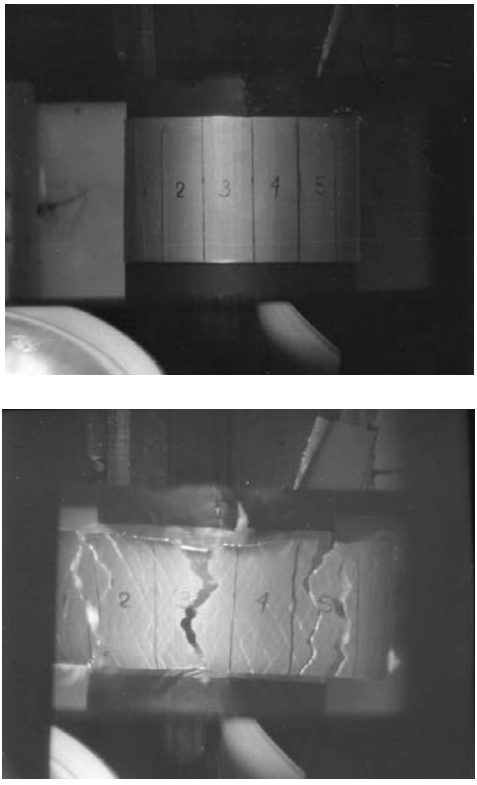

Fig. 8.18. High speed photograph illustrating deformation and fracture features in the expanding aluminum cylinder tests of Weisenberg and Sagartz (1977)

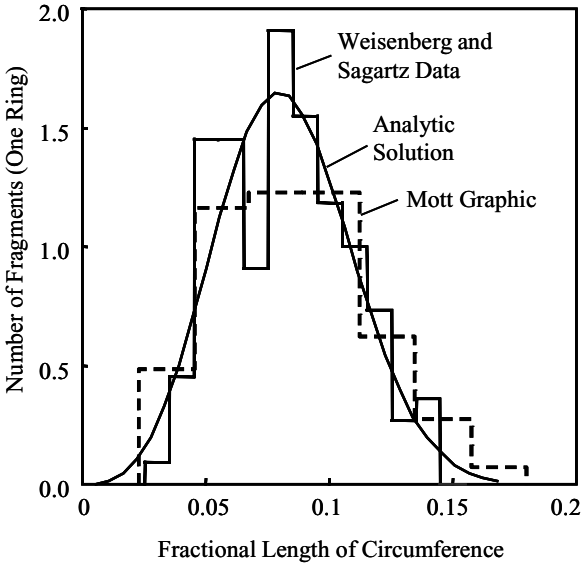

Fig. 8.19. Experimental fragment size data for expanding aluminum ring tests of Weisenberg and Sagartz (1977) and comparisons with statistical Mott theories

A total of 125 fragments were collected from 11 equivalent tests. All fragments were assigned an effective length by weight. Accordingly a histogram of the statistical size distribution for the aluminum cylinder data is provided in Fig. 8.19. In this figure the ordinate identifies the number of fragments normalized to a single ring which occurred within the corresponding fragment size (length) interval. The abscissa identified fragment size as a fraction of the original circumference of the ring.

Experimental fragment size data of Weisenberg and Sagartz (1977) in Fig. 8.19 are compared with both Mott's graphical distribution and the analytic distribution for plastic fracture developed previously in Sects. 3 and 4. Both distributions satisfactorily describe the relatively narrow spectrum of fragment lengths. It is straightforward to calculate the scatter in strain-to-fracture necessary within the Mott theory to account for the average fragment size displayed in the ring data. Using reasonable values of $Y = 300\,\mathrm{MPa}$ and $\rho = 2700\,\mathrm{kg/m^3}$ for 6061-T6 aluminum at an expansion strain rate of $10^4/\mathrm{s}$ a standard deviation in strain-to-fracture of about 0.25 is calculated from the Mott relation for fragment number. This estimated scatter in strain-to-fracture is probably not inconsistent with a nominal 0.3 strain-to-fracture determined in the experiments of Weisenberg and Sagartz (1977) although, it is somewhat larger than determined for 1100-O aluminum in the previous ring tests.

8.4 Winter's Expanding Cylinder

A further seminal experimental study of dynamic fragmentation performed in part to explore features of the Mott theory of fragmentation was conducted by Winter (1979). In that work thin cylinders (17 mm diameter and 1 mm wall thickness) of selected metals were loaded to fracture failure with a light gas gun. Metal cylinders were approximately half filled with an elastomeric material and nylon solid cylinder projectiles accelerated to velocities of several hundred meters per second were caused to enter the cylinder and strike the elastomeric material near the midpoint of the cylinder. Pressures brought about by the impact led to radial loading and plastic expansion of the metal cylinder. The intensity of the load and expansion speed of the cylinder was determined by the impact velocity of the nylon cylinder.

The test geometry and nature of the impact-induced deformation and subsequent failure are illustrated in Fig. 8.20. The cylinders experience rapid, relatively symmetric radial bulging at the waist. Radial velocity of the bulge extremum accelerates rapidly to a constant velocity and circumferential strain rates as determined from this velocity ranged from about 1×10^4/s to 4×10^4/s. Axial stretching rates within the bulge region were reported to be about one-third the circumferential strain rate.

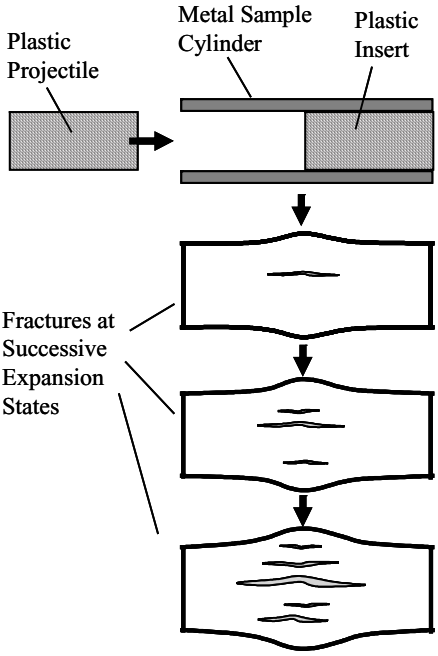

Fig. 8.20. Illustrated gun-accelerated-projectile technique for conducting dynamic expanding metal cylinder fracture experiments

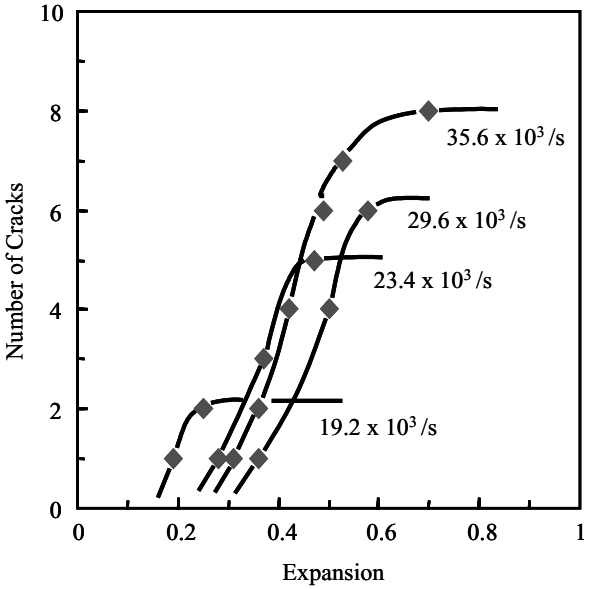

Fig. 8.21. Plot of fracture number as a function of cylinder expansion for the four experiments on naval brass of Winter (1979)

High-speed photography was the principal diagnostic providing deformation history as well as imaging inception and growth of axial fractures as dynamic deformation exceeded the failure limits of the material. Data are reported for aluminum, steel, copper, brass, and bronze. The more comprehensive study was that on naval brass. Metallurgical examination of fracture surfaces of recovered fragments revealed the shear fracture characteristics common to explosive fragmentation of metal shells.

Unique to this study was the effort to explore the temporal history of fracture inception. The multiple Kerr cell photographic images acquired at a rate of one every few microseconds (4 μs per frame was reported for the illustrated test on brass) provided a measure of the accumulation over time of the number of axial fractures participating in the failure process.

Results for the four tests on brass conducted by Winter (1979) at successively higher strain rates are shown in Fig. 8.21. Only fractures within the field of view imaged by the camera are included in this plot, which was approximately one-third of the cylinder.

This early study by Winter (1979) highlights a number of features unique to the failure of rapidly expanding ductile metal shells. The data focusing on the temporal history of fracture activation, is, however, absolutely unique and is central to the statistics-based fragmentation theory of Mott. Attention of the present efforts will address these data.

Each of the four tests on the brass cylinders shown in Fig. 8.21 illustrates the fact that the fractures responsible for cylinder failure do not all appear simultaneously but emerge statistically over time and expansion, in keeping with the statistical fracture criteria postulated by Mott. These data also illustrate that there is, in some sense, a measure of plastic strain incurred before fracture failure, although, a clear criteria for quantifying this strain-to-failure is less certain. Winter proposed a criteria based on a certain level of observable crack opening, which, from his plots of strain-to-failure, appears to correspond roughly to the cylinder expansion upon appearance of the last fracture. One might as readily propose strain-to-failure as the expansion upon appearance of the first fracture.

We will here also identify a strain-to-failure for the four experiments on naval brass for purposes of assessing the fragmentation theory of Mott. First, however, the theory will be pursued further to better understand the sense of strain-to-failure in Mott's statistics based theory. This pursuit will also reveal the coupling between the characteristic fracture spacing and the temporal occurrence of fractures necessitated by the theory of Mott and supported by the data of Winter.

In the earlier development of Mott's theory for ductile fracture in Chap. 3, the total number of fractures per unit circumferential length was provided through integration over all expansion $0 \leq \varepsilon < \infty$. Equally valid would be the expression providing the predicted number of fractures up to an expansion ε,

$$N(\varepsilon) = \frac{2n}{(2n+1)(a\sigma)^n} \int_0^y y^{\frac{2n}{2n+1}-1} e^{-y} dy \,, \tag{8.14}$$

where, $y = (a\varepsilon)^{(2n+1)/2}$ and with a provided in Sect. 3, where similar developments were pursued. The equation is readily integrated providing,

$$N(\varepsilon) = \beta_n \left(\frac{n}{\pi d^2 \sigma}\right)^{\frac{n}{2n+1}} G\left(\frac{2n}{2n+1}, y\right) \,, \tag{8.15}$$

where, β_n is the function of n provided in Chap. 3, and is sensibly unity for all n greater than one. The length scale $d = \left(2Y/\rho\dot{\varepsilon}^2\right)^{1/2}$and $G(\cdot, y)$ is the normalized gamma function, approaching unity as y approaches infinity.

A similar development can be put forth for the plastic strain accumulated through the cylinder expansion and fracture process. Early in the expansion before fracture initiates, expansion ε and the plastic strain ε_p are the same. When fractures initiate and Mott waves emanate from the points of fracture, regions encompassed by the waves will seize straining and the expansion and cumulative plastic strain will diverge. Analytically this is written,

$$\varepsilon_p(\varepsilon) = \int_0^\varepsilon (1 - D) d\varepsilon \,, \tag{8.16}$$

where, D is the fraction of circumference subsumed by Mott waves at expansion ε. This expression provides the integral,

$$\varepsilon_p(\varepsilon) = \frac{2}{(2n+1)a} \int_0^y y^{\frac{2}{2n+1}-1} e^{-y} dy \,, \tag{8.17}$$

with a and y the same as in the previous relations. Integration yields,

$$\varepsilon_p(\varepsilon) = \alpha_n \left(\frac{\sigma^n}{d}\right)^{\frac{2}{2n+1}} G\left(\frac{2}{2n+1}, y\right) \,, \tag{8.18}$$

where,

$$\alpha_n = \left(\frac{2}{2n+1}\right)^{\frac{2n-1}{2n+1}} \left[\frac{1}{\sqrt{\pi}} \frac{\Gamma(n+1/2)}{n\Gamma(n)}\right]^{\frac{2}{2n+1}} \Gamma\left(\frac{2}{2n+1}\right) \,, \tag{8.19}$$

is again close to unity for n greater than one.

Plots of the number of fractures and the cumulative plastic strain from (8.15) and (8.18) respectively, are shown in Fig. 8.22. The respective curves are normalized to σ and d equal to one, while $n = 7$ was chosen for illustration which corresponds to a standard deviation in the strain-to-fracture of $1.28\,\sigma/n$ or about 20%.

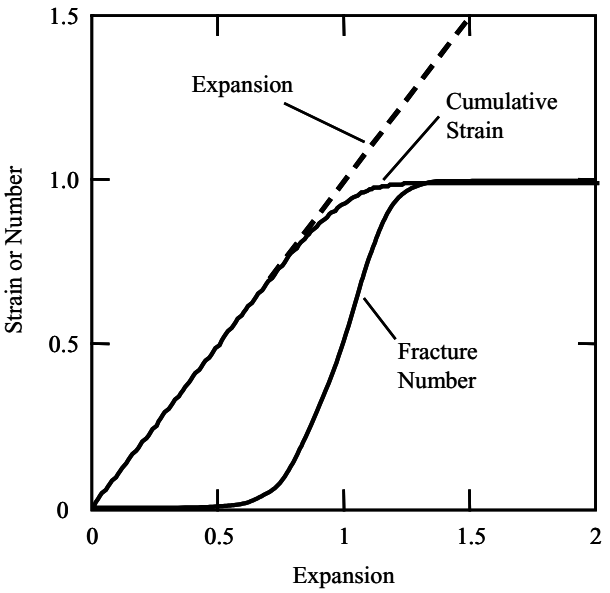

Fig. 8.22. Illustrates the temporal history of fragment number and cumulative plastic strain as a function of expansion

The plot illustrates the essential physics governing fragmentation in the Mott theory. Namely, the statistical spread in the strain-to-failure, governed by the parameter n when σ is fixed within a Weibull representation of the hazard function, determines both the characteristic fracture spacing (total fracture number) and the statistical temporal history of the appearance of fractures. Thus, within the Mott theory, the result of a certain characteristic fracture spacing requires a corresponding spread in the temporal occurrence of those fractures. The data of Winter (1979) for naval brass, in which both total fracture number and temporal history were measured, are therefore a unique and stringent test of the Mott theory.

In Fig. 8.22 the cumulative plastic strain is, according to the statistical Mott theory, observed to diverge smoothly from the cylinder expansion when fracture initiates and plateaus to a unique failure strain upon completion of the fracture process. The plot suggests that a reasonable observable estimate of the strain-to-failure is determined by the midpoint of the fracture number curve in the same plot. The data of Winter are consistent with this strain-to-failure interpretation.

Strain-to-failure by the above criteria as well as total fragment number for the four naval brass experiments of Winter (1979) are plotted as a function of expansion rate in Fig. 8.23. Assessing strain-to-failure from the midpoint of the number history curves in Fig. 8.21 reveals a degree of inconsistency in the data. Namely, the first (lowest expansion rate) and third test provide the lowest and the highest strain-to-failure, respectively, while the second and fourth are nominally the same. Error bars indicated in strain-to-failure are estimated from plotting uncertainties and photographic imaging frequency. These variations cannot be accounted for with Mott's statistics and perhaps relate to sensitivity of the dynamic fracture to preparation differences in individual

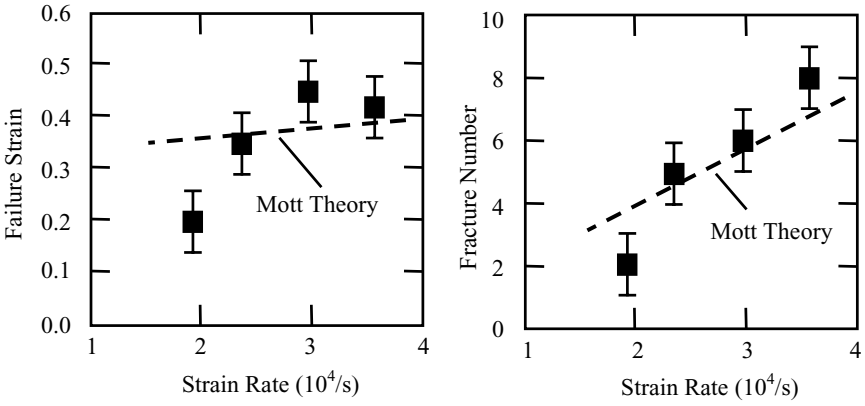

Fig. 8.23. Failure strain and fragment number from data of Winter (1979) on expanding naval brass cylinders. Curves represent the best fit with Mott fragmentation theory

cylinders (surface finish for example). In any case, these experimental variations in strain-to-failure are not captured in the theoretical representation to be described.

The fracture number data shown represent the fractures imaged by the photographic method over approximately a third of the circumference of the cylinder as described by Winter (1979). Error bars shown correspond to plus or minus one fracture.

Mott's theoretical equations for the total fracture number and the final strain-to-fracture ((8.15) and (8.18) for expansion approaching infinity) provided the best fit to the data in Fig. 8.23 by adjusting σ and n. The values were $n = 7$ and $\sigma = 0.18$ in S. I. units. A flow stress $Y = 300$ MPa and density $\rho = 8450\,\mathrm{kg/m^3}$ was used for the naval brass.

The statistical fracture number histories from (8.15) for the four experimental strain rates using the Mott parameters σ and n determined above from the final fracture number and plastic strain data for naval brass are shown in Fig. 8.24. Figures 8.23 and 8.24 clearly illustrate the coupling between final fracture spacing and the statistical appearance of fractures central to the theory of Mott. A comparison of the predicted histories of the fracture number in Fig. 8.24 with the experimental histories of Winter (1979) in Fig. 8.21 supports the Mott theoretical approach. Although the predicted curves cannot

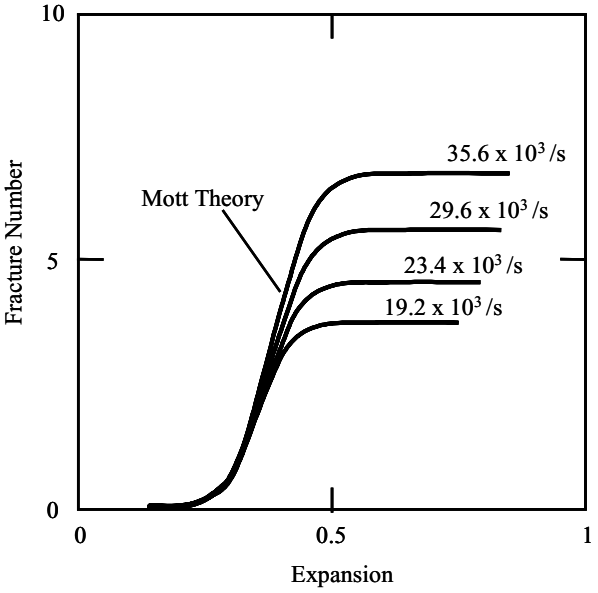

Fig. 8.24. Calculated fracture number history, or rate of fracture appearance, for the four naval brass experiments of Winter (1979) based on the Mott parameters n and σ selected to fit the fragment number and strain-to-fracture data

capture the scatter in translation of the several tests, the history of individual experimental tests is nicely reproduced by the theory.

8.5 Natural Fragmentation of an Exploding Cylinder

Smooth-walled explosively-loaded metal cylinders fragment without the aid of fragmentation enhancing techniques. In the natural fragmentation of exploding cylinders the statistical distribution in the size and velocity of fragments is determined thorough a complex interplay among explosive characteristics, geometry of the explosive-case system, and mechanical properties of the case metal. As noted in previous chapters, early attempts to introduce some scientific order to such violent event are attributed to Mott (1943, 1947, 1948), Taylor (1963), and Gurney (1943), among others. Chapter 7 of the present text is focused on issues of scaling of exploding cylinders. Literally thousand of arena tests of explosively-driven fragmenting cases in which various fragmentation data have been collected have been performed over the intervening decades.

In the present section discussion is focused on one study in which explosive and case metal were particularly well characterized, and quite thorough diagnostics were used to interrogate the explosive natural fragmentation event [Grady, and Hightower, 1992]. These results are considered in light of Mott's statistical and the energy-based predictions of fragmentation.

8.5.1 Natural Fragmentation Experiment

An explosive fragmentation experiment was performed on a 15.2 cm diameter smooth wall metal cylinder. The cylinder was 38.1 cm in length with a wall thickness of 5.7 mm. The cylinder was machined of 4140 steel and heat treated to a Rockwell hardness of 40 ($Y = 1.1$ GPa). The cylinder was filled with RX-35-AN explosive and the cylinder ends were confined. The explosive was center detonated at one end.

The insensitive high explosive RX-35-AN used in the present study has been calibrated through instrumented copper cylinder expansion experiments to provide expansion velocity data for purposes of establishing appropriate nonideal explosive equation-of-state parameters [Grady, 1990]. The measured expansion velocity data are scaled with appropriate Gurney relations to determine expansion velocity behavior for the steel cylinder experiment.

High speed front-lit photography using a CORDIN framing camera with 5 μs frame intervals was used to observe acceleration and breakup of the expanding cylinder. The opening of fractures and emergence of explosive gases were consistent with the 1.20–1.25 strain to fracture measured on recovered fragments. An expansion velocity of 1760–1830 m/s determined from the photographs compare well with the limiting Gurney velocity of about 1800 m/s calculated for this cylinder.

Multiple flash radiography was used to determine fragment velocity, trajectory and pattern for a 40° sector of the cylinder. Fragments from this sector were captured in fiberboard bundles which were placed approximately 6 meters from the event. From the bundles, 161 fragments were recovered which represents 90% of the weight of the 40° cylinder sector.

From the recovered fragments, it was observed that fracture was predominantly along elongated strips with the fracture parallel to the axis of the cylinder. A number of the fragments were 4 to 5 times longer than they were wide. Both tensile and shear fracture were observed from examination of fracture surfaces. Shear fracture appeared to be the dominant breakup mechanism. Fragment size statistics were determined from the recovered fragments for comparisons with the present fragmentation analysis.

8.5.2 Strain to Fracture

Within the fragmentation theories considered, it is necessary to establish the radial expansion velocity of the exploding cylinder at the moment of fracture to provide a measure of the strain rate at which breakup occurs. An early theory used to calculate the fracture strain of explosively expanding cylinders is due to Taylor (1963). Later improvements on Taylor's theory have been offered, however predicted fracture strains do not differ significantly from that of Taylor. Taylor's analysis led to a relation for the circumferential stress in the shell subjected to an internal pressure P given by $\sigma(y) = Y - P(1 - y/h)$ where Y is the yield stress in simple tension, h is the shell thickness and y *is* a coordinate through the thickness, $0 \leq y \leq h$. Thus $\sigma(0) = Y - P(\text{compression})$ at the inner surface and $\sigma(h) = Y(\text{tension})$ at the outer surface. The crossover point occurs at an interior point of the shell. Taylor assumed that failure occurs when the internal pressure within the expanding cylinder decreases to a value such that tension is just achieved at the inner surface.

It is common to assume ideal gas behavior for the explosive products and develop an expression for pressure versus expansion radius to calculate fracture strain with the Taylor method. The RX-35-AN explosive used in the present study was not suited to an ideal gas description of the explosive products, however. Instead, the velocity history data was used, through appropriate Gurney expressions, to calculate pressure versus radius behavior [Grady, 1990].

Through this method, an internal pressure of $P = Y = 1.1\,\text{GPa}$, corresponding to the yield stress of 4140 steel, is calculated at an expansion radius of $R/R_o = 1.24$. This fracture strain calculated through the Taylor criterion is compared with through-the-thickness measurements on a number of fragments recovered from the natural fragmentation experiment on the 4140 steel cylinder in Fig. 8.25. The comparison is reasonably consistent with the Taylor prediction.

Also shown is a best fit to the data of a Mott statistical strain to fracture function of the Gumbel type. The distribution curve required a mode,

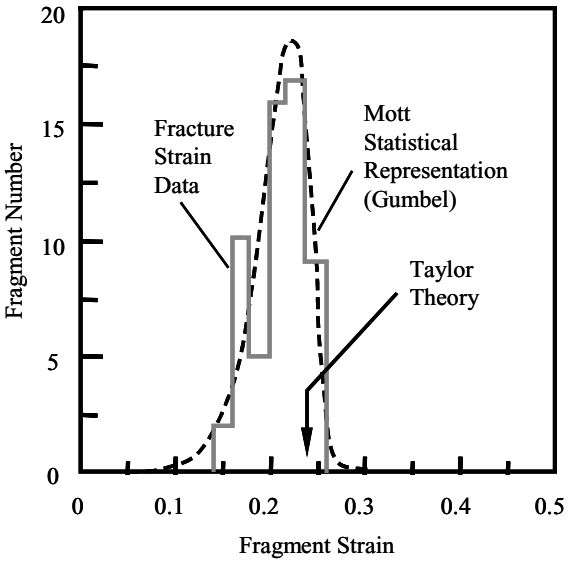

Fig. 8.25. Strain to fracture data from thickness measurements of individual fragments. Comparison with prediction of Taylor theory and a best fit to a Mott strain to fracture statistical distribution (Gumbel distribution)

$\mu = 0.22$, and scale parameter, $\sigma = 0.025$. (The standard deviation is $1.283\ \sigma$ whereas the Mott gamma parameter is $\gamma = 1/\sigma$).

The analyses of Gurney were then applied to determine the radial expansion velocity at the predicted fracture strain [Grady, 1990]. For the present experiment an expansion velocity of 1530 m/s was calculated. This value will be used in the subsequent fragmentation analysis to establish the strain rate at the time of fragmentation of $\dot{\varepsilon} \approx 1.6 \times 10^4/\text{s}$.

8.5.3 Fragment Size

Calculations of fragment size will be based on the several theoretical approaches considered in some detail in the earlier chapters. The statistics-based theory of Mott was found to provide a characteristic fracture spacing relation dependent on the current flow stress and circumferential strain rate, and on the spread in the strain to fracture (Mott's γ property) according to,

$$s = \sqrt{\frac{2Y}{\rho\dot{\varepsilon}^2}\frac{1}{\gamma}}\,, \tag{8.20}$$

Alternatively, an energy theory of fragmentation based on an extension of Mott's fracture interaction analysis [Kipp and Grady, 1985] including a fracture resistance property, leads to a circumferential fracture spacing of,

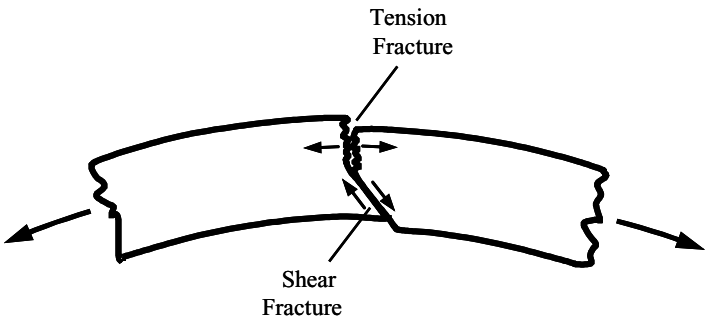

Fig. 8.26. Mechanisms of tension and shear fracture observed 4140 steel cylinder fragmentation

$$s = \left(\frac{24\Gamma}{\rho\dot{\varepsilon}^2}\right)^{1/3} , \tag{8.21}$$

where Γ is the fracture energy dissipated, and the work required, to compete the single fracture process. Comparisons of the present natural fragmentation data will be made with the several predictions of fracture spacing provided in (8.20) and (8.21).

8.5.4 Fragmentation Energy

Calculation of the nominal circumferential fracture spacing from (8.21) requires knowledge of the fragmentation energy Γ. The fragmentation energy is a material and mechanism dependent property which is determined through experimental measurements and models of the fracture dissipation process. There are two predominant modes of fracture in the breakup of an expanding metal shell which are illustrated in Fig. 8.26. The first is tensile fracture where failure proceeds by the opening of mode I cracks. Fracture dissipation is governed by the material fracture toughness K_c, and an estimate of the fragmentation energy is provided by,

$$\Gamma = \frac{K_c^2}{2E} , \tag{8.22}$$

where E is the elastic modulus of the material. Here it is assume that the static fracture toughness K_c provides a reasonable measure of the fragmentation toughness K_f. Material properties for the 4140 steel tested in the present study are provided in Table 8.2, and provide a fragmentation energy of $\Gamma \approx 16\,\mathrm{kJ/m^2}$ for tensile fracture.

In explosively-expanding cylinders, shear fracture preceded by localized adiabatic shear banding on the planes of fracture is also an important mode of failure. In determining the fragmentation energy associated with shear fracture, we will assume that the energy is principally accounted for by dissipation

Table 8.2. 4140 Steel Properties

ρ	(kg/m^3)	7870
Hardness	(HRC)	~ 40
E	(GPa)	200
K_c	(MN/m$^{3/2}$)	80
Y	(GPa)	1.1
χ	(m^2/s)	1.5×10^{-5}
c	(J/kg K°)	450
α	($K^{\circ -1}$)	7.5×10^{-4}
Γ Tensile	(kJ/m^2)	16
Γ Shear	(kJ/m^2)	19

in the adiabatic shear banding process. Grady and Kipp (1987) have analyzed the energy dissipated in adiabatic shear banding and have arrived at the expression,

$$\Gamma = \frac{\rho c}{\alpha} \left(\frac{9\rho^3 c^2 \chi^3}{Y^3 \alpha^2 \dot{\gamma}} \right)^{1/4} . \tag{8.23}$$

In (8.4), $\dot{\gamma}$ is the shear strain rate and is approximately equal to the circumferential stretching rate in the present application ($\approx 1.6 \times 10^4$/s). The new material properties include the specific heat c, the thermal diffusion coefficient χ, and the thermal softening coefficient α. From properties provided in Table 8.2 a fragmentation energy of $\Gamma \approx 19\,\mathrm{kJ/m^2}$ is obtained for shear fracture, which is remarkably close to that calculated for toughness governed tensile fracture.

Whether tensile or shear fracture dominated in the present fragmentation test on 4140 steel was not clear. Metallography on explosively fractured specimens indicated that this steel had a strong tendency to shear band and fracture along shear banded planes. There was also observation of fracture on planes oriented at approximately 45° to the shell surface, a further indication of shear dominated fracture. The close numerical values for the tensile and shear fragmentation energies will lead to similar predictions of circumferential fracture spacing, however. This similarity in magnitude of the two energy values is still not understood.

8.5.5 Distribution in Fracture Spacing and Comparison with Predictions

The present study is focused on predicting the circumferential fragmentation intensity. It does not consider axial breakup of the longitudinal strips. To make a statistical comparison of the fragment size data with the present analysis, the following reduction of the data was performed: Every fragment was weighed and the length of every fragment was measured. An effective rectangle was assumed for a fragment such that the mass is given by $m = \rho wtl$ where ρ is

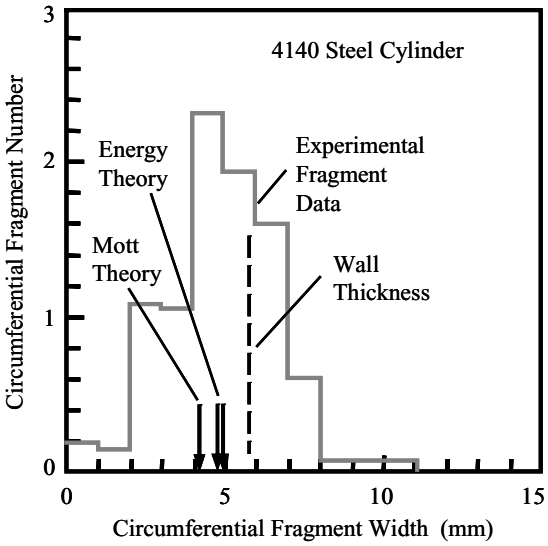

Fig. 8.27. Number histogram of the 161 fragments from the natural fragmentation of the 4140 steel cylinder and comparisons with predictions of circumferential fracture spacing

the density and w, t and l are the width, thickness and length, respectively. A circumferential fragment width was then calculated for each fragment from $w = m/\rho tl$ where m and l are the measured values and t is the initial wall thickness of the cylinder. The width w then provides an effective average measure of fracture spacing for that fragment in terms of the initial cylinder dimensions. A fragment of length l was then considered to be a fraction of a strip of length L, given by $n = l/L$, where L is the length of the cylinder. Through this method, a number versus circumferential width distribution was determined for the fracture spacing data.

The experimental circumferential fragment number data are plotted as a number histogram in Fig. 8.27. The same data are plotted as a cumulative number distribution in Fig. 8.28. The number data on the ordinate has been scaled from the 40 degree sector to a full cylinder. Initial wall thickness of the cylinder is identified in each figure for reference.

Predictions of the nominal fracture spacing based on the energy governed expression from (8.21) using both the tensile fracture energy ($\sim$16 kJ/m^2) and the shear band enhance fracture energy ($\sim$19 kJ/m^2) are identified in the figures. Specifically, the values are $s = 4.6$ mm (tension) and $s = 4.9$ mm (shear) referenced to initial circumferential dimensions. Predictions are slightly smaller than reported in Grady and Hightower (1992) because of a slightly different method of calculating the strain rate.

Fracture spacing predictions based on the Mott statistical theory through (8.20) additionally requires the γ property characterizing the statistical strain to fracture material behavior. Mott provided several methods for estimating γ. Here the statistical spread in fracture strain reported in Fig. 8.25 for the present fragmentation test will be used to determine γ. A value of $\gamma = 40$ calculated earlier in this section combined with the flow stress and density values from Table 8.2 yield a fracture spacing of 4.2 mm.

It is readily observed that all of the predicted values for fracture spacing are in sensible agreement with each other and the measured data. The 10% to 90% spread in fragment number ranges over about 3 mm and 7 mm easily spanning the predicted values. The close agreement between the energy-based prediction and Mott's statistics based prediction is intriguing and not fully understood. As discussed in Chap. 5, where the two theories are compared, the present agreement in predictions occurs in the regime of energy controlled fragmentation where Mott statistics is expected to characterizes the statistical fracture activation rather than the fracture survival and completion processes. This comparison also apparently carries over to the statistical variation in circumferential stretching, and corresponding fragment thickness strain, in the energy governed dynamic breakup process. Almost obscured in the data in Fig. 8.28 is a fit of the cumulative distribution with the Mott statistical fracture spacing distribution developed in Chap. 3. Again the agreement is surprisingly good. Disconcerting, however, is the observation that fracture

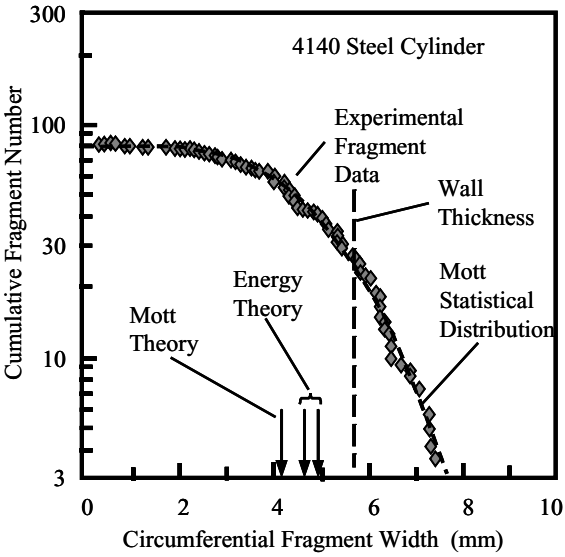

Fig. 8.28. Cumulative fragment number plot and comparisons with predicted fragment size and distribution

spacing in the present test span the thickness of the cylinder case bringing into question issues of thin case versus thick case behavior.

8.6 Tube Fragmentation Tests of Vogler and Coworkers

The seminal techniques developed by Winter (1979) have been revisited and extended in the dynamic fragmentation study of Vogler et al. (2003). Much of the early observations of Winter are supported in this extended investigation. Additionally, new results are reported due in part to the different materials studied and a broader range of diagnostic techniques.

8.6.1 Experimental Methods

Two well characterized metals were examined in this experimental study. The first was a heat treated AerMet 100 steel that has received considerable attention in fragmenting munitions applications [Wilson et al., 2001; Chhabildas et al., 2001]. Scaling studies of cylinder fragmentation performed on this steel are discussed in Chap. 7. The second is a highly ductile alloy of uranium, U6Nb, discussed in an early section in the present chapter.

The experimental test technique replicates much of that developed by Winter (1979). The test metals are produced in tubes 50.8 mm in length, 12.7 mm in inner diameter and with several tube wall thicknesses. Controlled inner loading is produced through a gas gun acceleration and insertion of a solid cylinder lexan projectile 25.4 mm in length striking an identical stationary lexan cylinder at the center point of the metal tube as previously illustrated in Fig. 8.20. The impact pressure and subsequent outward motion leads to dynamic budging of the metal cylinder causing in turn, rapid plastic straining, multiply dynamic fracture, and statistical fragmentation of the test metal.

Various diagnostic techniques were used to interrogate the dynamic failure and fragmentation process. High-speed photography provided detailed measurement of the expansion history along with the temporal evolution of dynamic fracture activation and propagation. Time resolved velocity interferometery or VISAR [Barker and Hollenbach, 1972] provided detailed expansion velocity history including initial shock intensity. PVDF pressure gages were mounted interior to measure impact generated pressure amplitude and quantitative pressure history of the cylinder loading function. Lastly, soft recovery methods captured fragment debris for post test evaluation and metallography.

8.6.2 Experimental Results

Results representative of the study are shown from high speed photographic imaging of the dynamic tests in Fig. 8.29. The images on the left are for a heat-treated AerMet tube with a 3 mm wall thickness. Comparable images for

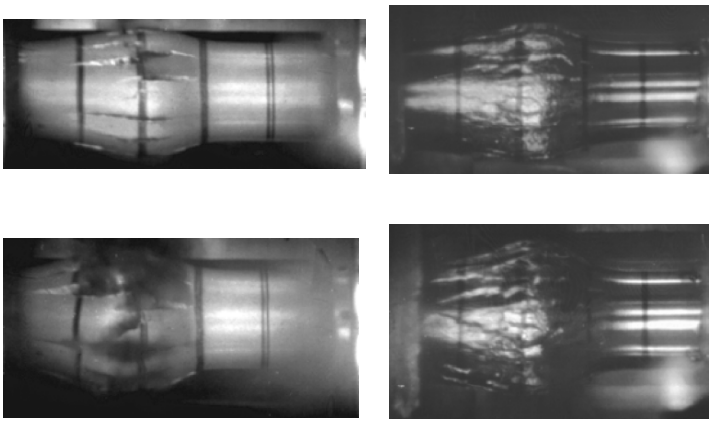

Fig. 8.29. The images on the left are for heat treated AerMet 100 steel at 15.4 µs and 23.4 µs after impact. Images on the right are for U6Nb uranium 18.3 µs and 25.1 µs after impact. Impact velocities were 1.92 km/s for steel and 1.86 km/s for uranium, respective

an experiment on a U6Nb tube are shown on the right. Timing of the images after impact are provided in the figure caption.

Initial expansion of the tube is visually homogeneous and cracking is not observed until some time after impact. For the one AerMet tube, fracture was first perceived at 10.4 µs after impact. This first observation corresponds to a circumferential strain at the maximum bulge of 18%. Comparable strains determined from the deformed thickness of collected fragments ranged over about 9% and 16%. Strains determined from the observation of first fracture on three U6Nb experiments were 12%, 21% and 24%, respectively. Strains inferred from fragments collected ranged over about 15% to 23%. Such scatter in strain to fracture should not be surprising and is consistent with similar results in the study of Winter.

After fractures become visible in the photographic imaging, their number increases rapidly. In the AerMet 100 experiment shown in the left of Fig. 8.29 a maximum of seven cracks were visible at 15.4 µs after impact. That number decreased, however, as the axially propagating cracks intersected and coalesced. The velocity of the principle cracks could be measured. Growth was not steady, especially immediately after activation, but measured velocities ranged from about 0.54 to 1.7 km/s. This crack speed compares with a Rayleigh wave speed for steel of 2.84 km/s.

The VISAR velocity profile measurements for comparable tests on AerMet steel and U6Nb uranium are shown in Fig. 8.30. The three VISAR locations are illustrated in the inset, and recorded radial motion at 5 mm intervals along the tube axis. Reverberation of the loading shock wave through the wall thickness is clearly observed as the radial acceleration proceeds. Maximum

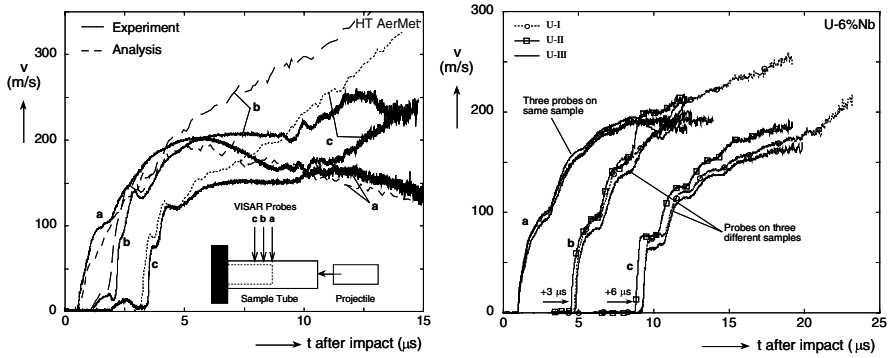

Fig. 8.30. Velocity measurements with VISAR for AerMet 100 steel (*left*) and U6Nb uranium (*right*) are shown as solid curves. CTH computational simulations are the broken curves compared with the measured data

radial velocity is achieved near the VISAR location b and is about 10% of the projectile impact velocity.

Computational simulations of the dynamic event were performed using the Sandia National Laboratories CTH shock physics code [Bell et al., 2000]. A Mie-Gruneisen equation of state model and von Mises ideal plasticity strength model were used for the participating materials. A Johnson-Cook fracture model [Johnson and Cook, 1983] was employed to determine fracture onset in the test metals. Simulations are compared with the measured velocity data in Fig. 8.30. Agreement with the data is reasonable although significant divergence at later time is observed. This discrepancy is attributed to both overly simplistic metal strength models, and to motion irregularities brought about by the statistical fracture and fragmentation process.

In selected tests under comparable impact conditions fragments from the dynamic event were soft recovered, counted and weighed. Fragment distribution data for one heat treated AerMet steel specimen and three U6Nb specimens are shown in Fig. 8.31. Cumulative fragment number is provided on the ordinate while cumulative fragment mass fraction (fraction of total tube mass) is shown on the abscissa. A representative fragment from each metal is also shown in the figure.

Typically a large section of the tubular specimen nearest the projectile insertion end remained intact. For the AerMet steel test provided in Fig. 8.31 this section was 48% of the whole tube mass. For the AerMet steel test fourteen fragments with mass greater that one gram were recovered. These fragments constituted the steeper portion of the distribution curve in Fig. 8.31. Thirteen smaller fragments were also recovered and complete the smaller particle shallow portion of the distribution curve. Steel fragments were generally elongated as the photograph illustrates in Fig. 8.31. Shear fracture at approximately 45 degrees to the surface normal was the rule. Fragments also exhibited crack steps and arrested fractures.

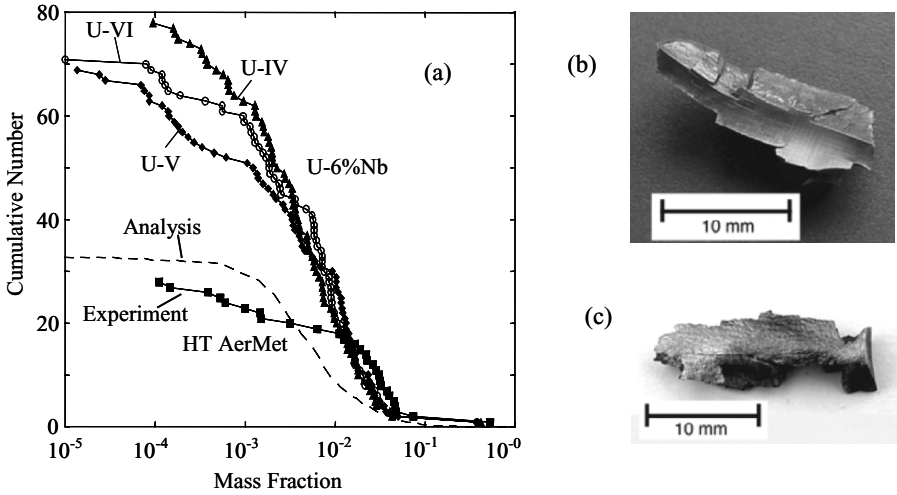

Fig. 8.31. Cumulative fragment number distributions versus fragment mass fraction for steel and uranium tube fragmentation tests. Representative recovered fragments for (**b**) heat treated AerMet 100 steel and (**c**) U6Nb uranium are also shown

The fragment mass distribution trend for U6Nb uranium, also shown in Fig. 8.31, is similar to that of steel but with markedly more fragments. Fragments were significantly more jagged and irregular, and tended to be more equi-dimensional. Significant deformation-induced surface roughening was also noted on the uranium fragments.

Fragment distributions for both the heat treated AerMet steel and U6Nb uranium were adequately fit to a bilinear distribution of the form,

$$N(m) = N_o^l e^{-m/\mu_l} + N_o^s e^{-m/\mu_s} \ . \tag{8.24}$$

Argument for the application of a bilinear mixture distribution are considered in Chap. 2 and have been discussed in earlier studies [Grady and Kipp, 1985; Odintsov, 1992]. Since large fragments dominate the distribution, the fitted distribution parameter μ_l was used along with the circumferential strain rate determined from VISAR or high-speed photography in the relation,

$$K_f = \sqrt{\frac{\rho c^2 \dot{\varepsilon}^2 \mu_l}{24}} \ , \tag{8.25}$$

to provide a measure of the effective fragmentation toughness under the present test conditions. For two AerMet heat-treated steel experiments strain rate at fracture of 5×10^4/s was determined and toughness values of 62 and 71 MPa $\mathrm{m}^{1/2}$ were obtained. For four U6Nb uranium tests the measured distributions provided toughness values of $49, 55, 58$ and $61\,\mathrm{MPa\ m}^{1/2}$. These values are remarkably close to the fragmentation toughness determined from expanding ring experiments on U6Nb discussed earlier in the present chapter.

8.6.3 Summary

The present extension of the expanding tube test technique initially explored by Winter (1979) is shown to provide a valuable method for investigating the phenomena of dynamic fracture and fragmentation. Additionally, barring the stochastic nature of dynamic fracture, the test method is found to be very reproducible, especially in the initial expansion phase of the tube. The method is quite amenable to the combined use of VISAR, high-speed photography and soft-recovery diagnostics.

The steel and uranium metals studied in the present investigation exhibit strikingly different fracture and fragmentation characteristics. Some of these features are not yet well understood. The outwardly more brittle fracture appearance and more abundant fragmentation of the uranium alloy was not expected but may relate to the propensity for this metal to undergo adiabatic shear failure.

The sensible agreement of the fragmentation toughness determined in the expanding tube method with other dynamic methods and with static fracture toughness values is encouraging. This agreement should be viewed with caution, however, as some of the assumptions important to the model are not realized in the expanding tube test. Nonetheless, the reasonable agreement among the different test methods suggest that the model must capture some of the physics reasonably well and should continue as a useful engineering tool.

8.7 Steel Cylinder Fragmentation of Mock and Holt

An instructive study of metal fragmentation is provided by the experimental investigation of Mock and Holt (1983) into the explosive-driven fragmentation of iron and steel cylindrical shells. In that study explosive loading was performed on the more ductile Armco iron and on HF-1 steel subjected to several heat treatments producing markedly more brittle response. Thick-walled test cylinders provided large numbers of fragments, and well-constrained fragment distributions. The study also included a detailed examination of fragment morphology and provided a classification scheme for the sorting of fragments. Both distributions and fragment classification provide unique data for testing statistical theories and examine the physical processes governing dynamic fracture over several ferrous metals with different fracture characteristics.

8.7.1 Experimental Methods

Explosive fragmentation tests were performed on metal open-end cylindrical shells approximately 20 cm in length, 7.5 cm in inner diameter and 2 cm in wall thickness. The explosive was cast-in-place composition B explosive which

was detonated at one end and extended well beyond each end of the metal cylinder.

The first metal was as-received Armco iron. The second, was an HF-1 steel heat treated to a tempered martensite state. The third, was also HF-1 steel heat treated to a more brittle cementite and pearlite structure. Six fragmentation tests, two on each metal, were performed. Fragments were soft captured in sawdust and extracted with magnetic methods. Over 99% of the original cylinder mass was recovered on all tests. Over 1400 fragments weighing more that 1 gr (0.065 g) were collected from the Armco iron tests and contributed to the data analysis. Similarly, over 10,000 and 12,000 fragments, respectively, were collected for the two heat treatments of HF-1 steels.

8.7.2 Fragment Distributions

Cumulative fragment number greater than mass m versus fragment mass is plotted in Fig. 8.32 for both experiments on Armco iron. Separate symbols are not used to distinguish between the two tests because they overlay within the statistical scatter. One curve in the figure represents the distribution of all (total) of the fragments collected. The other curve identifies the distribution of specific type 1 fragments which will be described shortly.

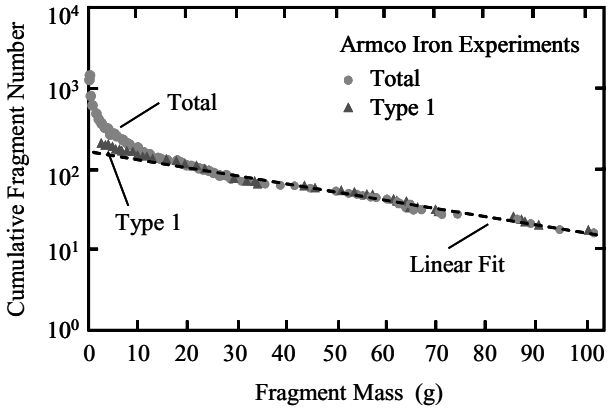

Fig. 8.32. Fragment mass distributions for Armco iron exploding cylinder tests [Mock and Holt, 1983]

In Fig. 8.33 similar fragment distributions are shown for the total number of fragments for the first (heat treatment A) and second (heat treatment B) preparations for the HF-1 steel. Again, two tests were performed on each heat treatment, so the two curves represent the resulting distributions for approximately 21,000 and 25,000 fragments, respectively.

It was pointed out by Mock and Holt (1983) that the distributions in Figs. 8.32 and 8.33 for the total number of fragments were well described

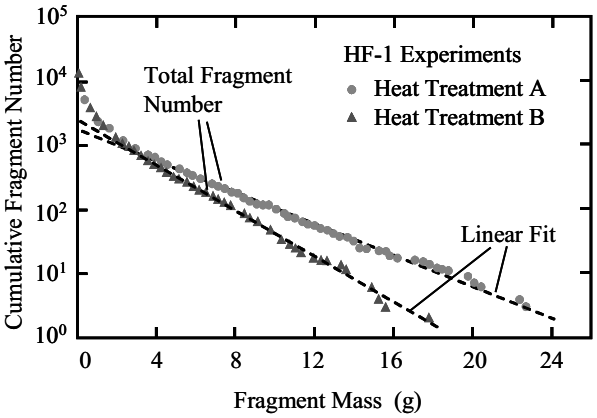

Fig. 8.33. Fragment mass distributions for HF-1 steel exploding cylinder tests [Mock and Holt, 1983]

with a linear curve in these semi logarithmic plots with the exception of the upturn associated with the smaller fragment end of the distribution. These curves would correspond to $\beta = 1$ for the general scaling relation suggested in Chap. 7. Grady and Kipp (1985) have shown that the data of Mock and Holt are very well described by a bilinear exponential, or Poisson mixture, distribution as described in Chap. 2.

8.7.3 Fragment Morphology

A further feature of the study of Mock and Holt (1983) was the classification of fragments according to the shape and the mode of fracture governing the fragment separation process. The author's noted that attempts to type sort fragments resulting from exploding munitions events goes back to at least the early reports of Mott. Several of these reports by Mott do in fact examine the shape and fracture surface features of collected fragments, and comment on the several fracture processes possibly responsible. In Fig. 8.34 sketches from the report of Mott are reproduce and illustrate the classification of fragments observed by him. He suggested that failure probably initiated on the inner surface of the munition cylinder as shear rupture, transitioned to extension fracture at some interior point, and culminated at the cylinder outer surface. In his observations, fragments of type 1–4 were commonest with occasional fragment of type 5. He also pointed out that for mild steel and carbon steel, through-going shear rupture was frequently observed as illustrated in his lower sketch in Fig. 8.34.

Mock and Holt (1983) found the more extensive fragment classification scheme shown in Fig. 8.34 more appropriate to the Armco iron and HF-1 steel cylinder tests performed by them. This method suggested four principle fragment types comprised of type 1 fragments (including both inner and

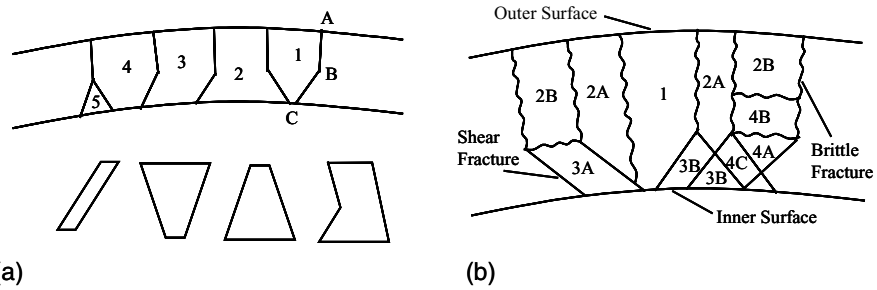

Fig. 8.34. Classification schemes for fragment type resulting from exploding munitions fragmentation. (**a**) Original sketches of Mott (1943). (**b**) Fragmentation classification of Mock and Holt (1983)

outer cylinder surfaces), type 2 (outer cylinder surface only), type 3 (inner cylinder surface only), and type 4 (no cylinder surface). Fragments were further subtyped according to the shear or extension character of the fracture surfaces.

Sorting of the fragments according to this scheme was carried out for the tests performed. It was shown that for the more ductile Armco iron fragments of type 1 (both inner and outer fragment surface) constituted very close to 80% of the total cylinder mass. The authors further showed that the distribution for only the type 1 fragments for the Armco iron tests plotted linear on a semi logarithmic cumulative number versus mass graph over the full range of the data as illustrated in Fig. 8.32. Fragments of the remaining type contributed to the small mass upturn adequately described by a bilinear exponential distribution. Behavior is reminiscent of the cylinder tests of Odintsov (1992) discussed in Chap. 2.

Sorting of fragments from tests on HF-1 steel, on the other hand, resulted in less than 5% of the mass of type 1 fragments. A complex mix of fragments of type 2 through type 4 constituted the preponderance of the fragment mass distribution.

A final noteworthy observation in the tests of Mock and Holt were correlations among static strength properties of the several metals and features of the fragmentation results. Armco iron provided a tensile strength of approximately 300 MPa and a permanent elongation to fracture of 34%. In contrast, the two heat treatments of HF-1 steels, A and B, respectively, exhibited 1100 MPa and 880 MPa tensile strengths and elongations to fracture of 3% and 1%. Some variations in properties with respect to orientation relative to rolling direction were noted, however.

For comparison, expected fragment mass for the fragment distributions for Armco iron and for the HF-1 steel with heat treatments A and B were $\mu = 41\,\mathrm{g}$, $3.6\,\mathrm{g}$ and $2.5\,\mathrm{g}$ respectively, based on a linear exponential description of the linear portion of the respective distributions. Estimating a circumferential strain rate from Gurney considerations of approximately $10^4/\mathrm{s}$ the

respective mass scale parameters in (8.25) of the previous section yield fragmentation toughness values of $K_f = 185, 55$, and 45 MPa $m^{1/2}$, respectively for the three metals.

Type 1 fragments which were large enough to include both inner and outer surfaces of the original cylinder were examined to infer other feature of the dynamic fracture event. These included all of the type 1 fragments from each of the HF-1 steel experiments (approximately 25 to 50 fragments per test) and a comparable representative number from the Armco iron tests. A permanent dynamic strain to fracture was estimated from the change in thickness relative to the initial cylinder wall thickness. These engineering strain values were 0.34 and 0.36 for the two Armco iron tests, 0.11 and 0.12 for HF-1 steel heat treatment A, and 0.12 and 0.14 for heat treatment B.

Lastly the authors showed that the extent of shear fracture through the thickness before transition to the more brittle extension fracture behavior was dependent on the metal properties. For Armco iron shear fracture proceeded through nearly one-half (approximately 45%) of the cylinder wall thickness before transitioning to extension fracture. For the two HF-1 steels this shear fracture distance was reduced to about 25% and 20% of the wall thickness for heat treatments A and B, respectively.

References

Addesssio, F.L., Zuo, Q.H., Mason, T.A. (2003) Model for High-Strain-Rate Deformation of Uranium-Niobium Alloys, *J. Appl. Phys.*, 93, 12, 9644–9654.

Barker, L.M., and Hollenbach, R.E. (1972) Velocity Interferometer for Measuring the Velocity of any Reflecting Surface, *J. Appl. Phys.*, 43, 4669–4680.

Bell, R.L., Baer, M.R., Brannon, R.M., Elrick, M.G., Hertel, E.S., Silling, S.A., Taylor, P.A. (2000) CTH User's Manual and Input Instructions, Version 4.00, Sandia National Laboratories Tech. Rept., April.

Chhabildas, L.C., Reinhart, W., Wilson, L.T., Reedal, D.R., Grady, D.E., Black, J.W. (2001) Fragmentation Properties of AerMet 100 Steel in Two Material Conditions in Proceedings 19^{th} International Symposium on Ballistics, Interlaken, Switzerland, May 7–11, I.R. Crewther, ed., 663–670.

Gourdine, W.H. (1989) *J. Appl. Phys.*, 65, 411.

Gourdine, W.H., Weinland, S.L., Boling, R.M. (1989) *Rev. Sci. Inst.*, 60, 427.

Grady, D.E. (1990) Natural Fragmentation of Conventional Warheads, Sandia National Laboratories Technical Report SAND90–0254, May 1990.

Grady, D.E. and Benson (1983) Fragmentation of Metal Rings by Electromagnetic Loading, *Experimental Mechanic*, 23, 393–400.

Grady, D.E. and Kipp, M.E. (1985) Geometric Statistics and Dynamic Fragmentation, *J. Appl. Phys.*, 58, 3, 1210–1222.

Grady, D.E. and Kipp, M.E. (1987) The Growth of Unstable Thermoplastic Shear with Applications to Steady-Wave Shock Compression in Solids, *J. Mech. Phys. Solids* 35, (1), 95–118.

Grady, D.E. and Hightower, M.M. (1992) Natural Fragmentation of Exploding Cylinders, in Shock-Wave and High-Strain-Rate Phenomena in Materials, and K.P. Staudhammer, eds., Marcel Dekker, Inc., 713–721.

Grady, D.E. and Olsen, M.L. (2003) A Statistics and Energy Based Theory of Dynamic Fragmentation, *In. J. Impact Eng.*, 29, 293–306.

Gurney, R.W. (1943) The Initial Velocity of Fragments from Bombs, Shells and Grenades, Army Ballistic Research Laboratory Report BRL 405.

Hixson, R.S., Vorthman, J.E., Zurek, A.K. Anderson, W.W., Tonks, D.L. (2000) Spall Response of U-NB (6%) Alloy, in Shock Compression of Condensed Matter, – 1999, edited by M.D. Furnish, L.C. Chhabildas, R.S. Hixson, *Am. Inst. Physics*, New York, pp. 489–492.

Hogatt, C.R. and Recht, R.F. (1969) Stress Strain Data Obtained at High Rates Using an Expanding Ring, *Experimental Mechanic*, 9, 441–448.

Johnson, G.R. and Cook, W.H. (1983) A Constitutive Model and Data for Metals Subjected to Large Strains, High Strain Rates and High Temperatures, Proceedings Seventh International Symposium on ballistics, The Hague, The Netherlands.

Kipp, M.E. and Grady, D.E. (1985) Dynamic Fracture Growth and Interaction in One Dimension, *J. Mech. Phys. Solids* 33 (4), 399–415.

Kipp, M.E. and Grady, D.E. (1986) Random Flaw Nucleation and Interaction in One Dimension in Metallurgical Applications of Shock-Wave and High-Strain-Rate Phenomena, L.E. Murr, K.P. Staudhammer, and M.A. Meyers, eds., Marcel Dekker, Inc., 781–791.

Mock, W. and Holt, W.H. (1983) Fragmentation Behavior of Armco Iron and HF-1 Steel Explosive Filled Cylinders, *J. Appl. Phys.*, 54, 2344–2351.

Mott, N.F. (1943) Fragmentation of H.E. Shells: A Theoretical Formula for the Distribution of Weights of Fragments, *Ministry of Supply*, AC3642, March.

Mott, N.F. (1943) A Theory of the Fragmentation of Shells and Bombs, *Ministry of Supply*, AC4035, May.

Mott, N.F. (1947) Fragmentation of Shell Cases, *Proc. Royal Soc.*, A189, 300–308, January.

Mott, N.F. (1948) Fracture of Metals: Theoretical Considerations, *Engineering*, 165, 16–18.

Odintsov, V.A. (1992) Hyper Exponential Spectra of Exponential Fracture, *Mechanics of Solids*, (Meckhanika Tverdogo Tela), 27, 5, 42–48.

Olsen, M.L. (2000) Private Communication.

Perrone, N. (1968) On the Use of the Ring Test for Determining Rate-Sensitive Material Constants, *Experimental Mechanic*, 8, 232–236.

Taylor, G.I. (1963) Scientific Papers of G.I. Taylor, Volume III, No. 44, Cambridge University Press.

Vogler, T.J., Thornhill, T.F., Reinhart, W.D., Chhabildas, L.C., Grady, D.E., Wilson, L.T., Hurricane, O.A., Sunwoo, A. (2003) Fragmentation of Materials in Expanding Tube Experiments, *Int. J. Impact Eng.*, 29, 735–746.

Walling, H.C. and Forrestal, M.J. (1973) Elastic Plastic Expansion of 6061-T6 Aluminum Rings, *J. AIAA*, 11, 1196.

Warnes, R.H., Duffy, T.A., Karpp, T.A., Carden, A.E. (1981) An Improved Technique for Determining Dynamic Material Properties Using the Expanding Ring, *in Shock Waves and High-Strain-Rate Phenomena*, M.A. Meyers and L.E. Murr, eds., Plenum, 47.

Weisenberg, D.L., and Sagartz, M.J. (1977) Dynamic Fracture of 6061-T6 Aluminum Cylinders, *J. Appl. Mech.*, 44, 643.

Wilson, L.T., Reedal, D.R., Kipp, M.E., Martinez, R.R., Grady, D.E. (2001) Comparison of Calculation and Experimental Results of Fragmenting Cylinder Experiments, in Shock Waves and High Strain Rate Phenomena, K.P. Staudhammer, M.A. Meyers, L.E. Murr, eds., Elevier, pp. 561–570.

Winter, R.E. (1979) Measurement of Fracture Strain at High Strain Rates, *Inst. Phys. Conf. Ser.* 47, 81–89.

Zurek, A.K., Hixson, R.S., Anderson, W.W., Vorthman, J.E., Gray, G.T., Tonks, D.L. (2000) Elastic Response of U-Nb (6%) Alloy, Proceedings 6th International Conference on Mechanical and Physical Behaviour of Materials under Dynamic Loading, Sept. 25–29, EDP Sciences, 677–682.